JOURNAL OF ELECTRON MICROSCOPY TECHNIQUE 9:325–358 (1988)

STEL 88

# Computer Image Processing of Electron Micrographs of Biological Structures with Helical Symmetry

MURRAY STEWART
*Medical Research Council, Laboratory of Molecular Biology, Cambridge CB2 2QH, England*

*KEY WORDS* Filtering, 3-D reconstruction, Viruses, Filaments, Flagella, Fourier transform

*ABSTRACT* Methods are described for the analysis of electron micrographs of biological objects with helical symmetry and for the production of three-dimensional models of these structures using computer image reconstruction methods. Fourier-based processing of one- and two-dimensionally ordered planar arrays is described by way of introduction, before analysing the special properties of helices and their transforms. Conceiving helical objects as a sum of helical waves (analogous to the sum of planar waves used to describe a planar crystal) is shown to facilitate analysis and enable three-dimensional models to be produced, often from a single view of the object. The corresponding Fourier transform of such a sum of helical waves consists of a sum of Bessel function terms along layer lines. Special problems deriving from the overlapping along layer lines of terms of different Bessel order are discussed, and methods to separate these terms, based on analysing a number of different azimuthal views of the object by least squares, are described. Corrections to alleviate many technical and specimen-related problems are discussed in conjunction with a consideration of the computer methods used to actually process an image. A range of examples of helical objects, including viruses, microtubules, flagella, actin, and myosin filaments, are discussed to illustrate the range of problems that can be addressed by computer reconstruction methods.

## INTRODUCTION

Computer image processing has been a powerful tool in the investigation of helical assemblies of biological macromolecules and has often provided spectacular insights into their structure and arrangement that cannot be obtained by simple inspection. Because the patterns from the top and bottom of helices overlap, an interference pattern is usually produced in which it is difficult to make out the subunit positions or their shape. Computer methods enable these problems to be circumvented and, moreover, enable three-dimensional models of the structures to be easily produced, often from a single view. In this way, new insights have been obtained on the structure of objects such as filamentous viruses, muscle and cytoskeleton filaments, bacterial flagella, and nucleosomes.

This article reviews computer image processing of biological objects with helical symmetry. It is assumed that the reader is familiar with the elements of Fourier-based image processing applied to planar objects, such as two-dimensional crystals, and so this article will concentrate on the specific properties of helices; the methods used to process images of helical objects; and some illustrative examples of the results that can be obtained. Readers not intimately familiar with image processing of planar objects are referred to the companion article in this volume (Stewart, 1988) and to a number of recent reviews of the subject (for example, Aebi et al., 1984; Amos, 1974; Stewart, 1986); only a brief introduction to these methods will be given here. Before proceeding to discuss the

Received March 31, 1987; accepted August 26, 1987.

Address reprint requests to Dr. Murray Stewart, Medical Research Council, Laboratory of Molecular Biology, Hills Road, Cambridge CB2 2QH, England.

image processing of helices, it is, however, helpful to consider the general nature of helical symmetry and to appreciate why biological objects with this symmetry are so often found.

## HELICAL STRUCTURES

A wide range of biological assemblies are constructed from subunits arranged in a regular manner. These structures usually take the form of two- or three-dimensional crystals, helices, or shells. This arrangement is because, in these sorts of structure, each repeating unit is located in an equivalent environment (at least approximately), and so the interactions between subunits are always the same (Caspar and Klug, 1962). This is important, because it means that only a small number of interaction surfaces need to be specified. If the contacts between subunits in a large assembly were all different, a very large number of interaction surfaces would have to be specified, which would greatly increase the complexity of the structure of the individual units. Thus assemblies in which the units are equivalent require much less information to specify their structure and can easily self-assemble.

Helices and shells can be thought of as special cases of two-dimensional crystals, in which the crystalline sheet has been deformed into a cylinder or a sphere, respectively. These structures seem to occur naturally in biological systems with rather greater frequency than crystals, possibly because helices and shells are bounded in two and three dimensions, respectively, and so have more defined limits placed on their size and growth. Aggregates of this form have been adapted to serve a broad range of roles. Virus capsids, for example, are frequently helical or icosahedral shells. Helices also find a more general application when elongated structures are required, since, although their diameter is fixed, helices can be extended more or less indefinitely. Examples of naturally occurring helical structures include DNA, viruses, cytoskeletal and muscle filaments, flagella, and the α-helix that forms an important component of protein secondary structure. In addition, biologically interesting molecules can sometimes be induced to form helical aggregates or bind to helical structures, thereby facilitating analysis by electron microscopy and X-ray diffraction. Examples of the latter sort of aggregate include nucleosomes (Klug et al., 1980), decorated muscle thin filaments (Taylor and Amos, 1981), glutamate synthetase (Frey et al., 1975), catalase (Kiselev et al., 1968), and the *rec*A protein (Egelman and Stasiak, 1986).

Helical objects can often be ideal objects for analysis by electron microscopy and computer image processing because they have particular properties that make it relatively straightforward to obtain a three-dimensional view of the subunit, at least at moderate resolution (about 2 nm). However, although this analysis is direct and quantitative, it does require some considerable care and also an understanding of the special properties of helices and their Fourier transforms. Some aspects of this theoretical basis for processing helical particles are different from the concepts generally employed for planar crystalline arrays. Moreover, some of the differences are rather subtle and can easily confuse even experienced workers. Consequently, before reviewing the methods employed in analysing helical particles, some space will be devoted to explaining the basis of the method and to examining some of the special properties of helices and their transforms. Because many readers of this article will probably be biologists without a deep background in mathematics, emphasis will be placed on geometric properties and the manner in which the problem should be conceived. Although equations are also provided, one need not worry unduly about detailed derivations provided the basic concepts are understood, since computer programmes are available to carry out the detailed calculations. There have also been a number of helpful reviews covering the mathematical basis of image processing to which the reader is directed (Aebi et al., 1984; Amos, 1974; Amos et al., 1982a; DeRosier and Moore, 1970; Fraser and MacRae, 1973; Misell, 1978; Stewart, 1986).

## BACKGROUND TO IMAGE PROCESSING

Image processing is a powerful adjunct to electron microscopy when investigating the structure and arrangement of biological macromolecules and subcellular assemblies. These methods aim to alleviate many of the problems generally present in electron micrographs of biological material and thereby enable higher-resolution structural information to be extracted and analysed. In this way, a more quantitative view of the struc-

ture is often produced than is obtained by simple inspection. Thus high-resolution features or small differences between objects that are usually masked by poor contrast and granularity from stain and support film can be reliably delineated; confusion caused by superposition of information from different levels of the object resolved; and often a three-dimensional model produced to overcome the inherently limited two-dimensional view obtained by electron microscopy. Ideally most of these methods can be applied to any general object, but the methods are usually most powerful when applied to regular objects, such as crystals, helices, or shells. This article will concentrate mainly on helical objects; the application of these methods to two-dimensional crystals is treated elsewhere (for example, Aebi et al., 1984; Amos, 1974; Stewart, 1986; 1988).

Image processing of regular two-dimensional crystals relies on the particular property that the Fourier transform of such an object is concentrated into a number of spots, placed on a lattice that is related to the original crystal lattice. Background "noise" is, by contrast, distributed over the entire Fourier spectrum, and this enables noise to be filtered out of images, which can result in a dramatic enhancement of fine structural detail (see, for example, Stewart, 1988). To process images digitally, it is necessary to first convert them into a numerical form suitable for computer analysis, using a digitiser that scans the negative in a raster pattern and records the densities at regular intervals over the area to be processed. These data are stored on magnetic disc or tape until required for processing, which is usually carried out along the lines suggested by DeRosier and Moore (1970). Fourier transforms are calculated using standard fast algorithms (Cooley and Tookey, 1965; Fraser, 1974) and displayed using either line printers or raster graphics devices. The required parts of the transform are then selected and averaged internally according to the symmetry of the object or with data from other micrographs if required, and a filtered image is reconstructed by Fourier synthesis. The filtered image is displayed either graphically (often using contour plots for two-dimensional objects) or on a raster graphics device. Figure 1 shows a flow chart of the basic steps in this procedure.

Electron micrographs of biological material can sometimes be made difficult to interpret by the interference of information from different structural levels in the object. Because the depth of focus in the electron microscope is large compared with specimen thickness, all levels of the object will be in focus simultaneously. Thus, if two regular layers overlap, their lattices will be superimposed in the image; this produces moiré patterns that make it difficult to ascertain the structure of each lattice by simple inspection. If the lattices are rotated relative to each another, it is usually possible to separate the contributions of each layer in the Fourier transform, since most reciprocal lattice points from one layer usually do not overlap with those from the other. Thus, provided that the contributions from each layer can be identified, an image of a single layer can be produced by Fourier synthesis. Figure 2 illustrates how this can be done. Note that, in this instance, not only has noise been removed by filtering, but so has the contaminating periodic structural information from the other regular layer. It is sometimes possible to separate the contributions from overlapping layers that are related by translation rather than rotation. However, this requires some knowledge of the structure of the underlying individual layers, since the spots from each reciprocal lattice now overlap. Least squares analysis can be employed to decompose the composite pattern and show, at least, that it is consistent with two overlapping layers, as was done, for example, with the double surface layer of *Aquaspirillum serpens* MW5 (Stewart and Murray, 1982).

A common source of superimposed lattices is the collapse of a cylinder, as happens often, for example, when dried in preparation for electron microscopy. A moiré pattern then forms between the top and bottom of the flattened tube. The classic example of this sort of pattern is that found in bacteriophage T4 polyheads (Laemmli et al., 1976; Steven et al., 1976; Yanagida et al., 1972), but other more recent examples include tubes of actin (Aebi et al., 1981), acetyl choline receptors (Brisson and Unwin, 1984), sarcoplasmic reticulum ATPase (Buhle et al., 1983; Castellani and Hardwicke, 1983; Taylor et al., 1984), cytochrome reductase (Leonard et al., 1981), and myosin subfragment-2 (Quinlan and Stewart, 1987). A naturally occurring example is the sheath of *Methanospirillum hungatei*

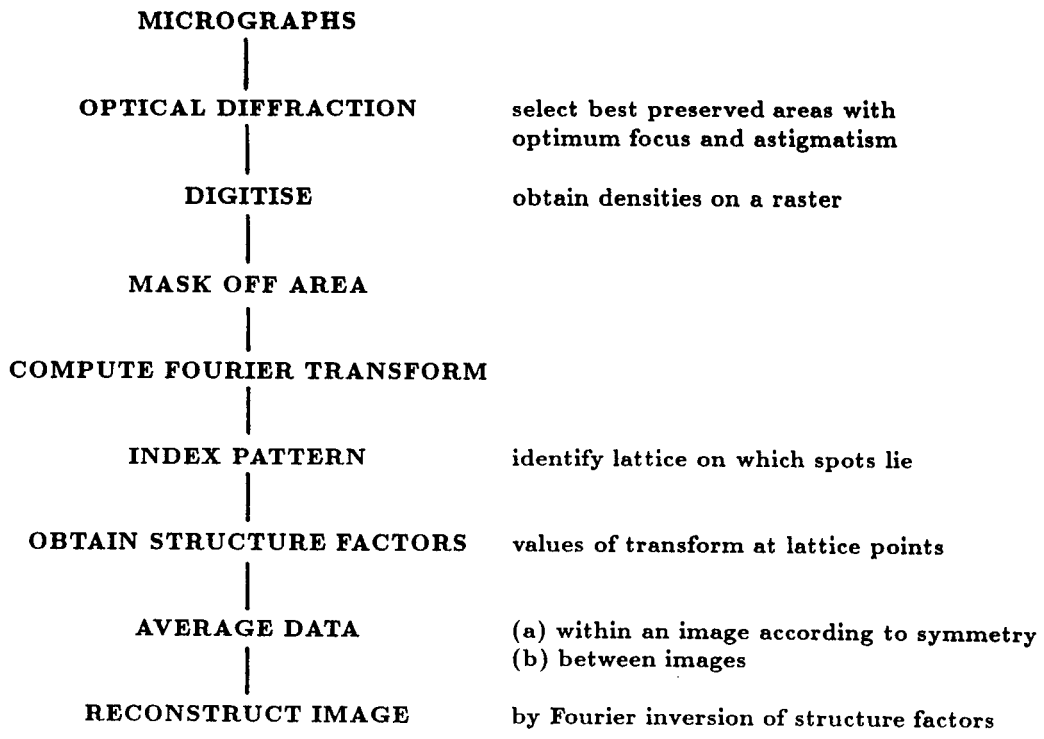


Fig. 1. Flow chart for Fourier-based image processing of regular one- and two-dimensional planar objects.

(Stewart et al., 1985a). In all these examples, the lattices from the top and bottom were rotated relative to one another, and so views of a single side were easily produced by filtering.

Helices are, of course, unflattened cylinders, and consequently these objects also suffer from interference between patterns on their upper and lower surfaces. This can often make it difficult to decide, by visual inspection, even their symmetry, let alone the shape or orientation of their subunits. However, it is, in principle, possible to separate the contributions from top and bottom and so reconstruct single-sided images that allow these features to be appreciated more fully (DeRosier and Klug, 1968). An example of this sort of analysis is shown in Figure 3. However, the Fourier transform of helical objects is somewhat different from that of plane layers, and so it is necessary to examine the properties of helical objects and their Fourier transforms in some detail before proceding to a discussion of the methods employed to analyse and process these objects.

## HELICES AND THEIR FOURIER TRANSFORMS

Helices can be considered as being formed from a regular two-dimensional lattice rolled into a cylinder, as illustrated in Figure 4. In addition, whereas the thickness of a two-dimensional crystal can be thought of as being built up from a number of thin sheets stacked on top of one another, a helical structure can be considered as a series of thin coaxial cylinders. *This conceptualisation is central to the discussion of helices and their transforms. It forms the basis of computer methods used to analyse these structures and produce filtered images and three-dimensional reconstructions from electron micrographs.*

If one conceives of a helix as a planar lattice rolled into a cylinder, then one can also describe the variation of density in the structure in terms of an analogous sum of waves. However, these will be *helical waves* following helical tracks, rather than the plane waves following linear tracks that were employed in planar objects (Fig. 5). A helical wave is simply formed by rolling a

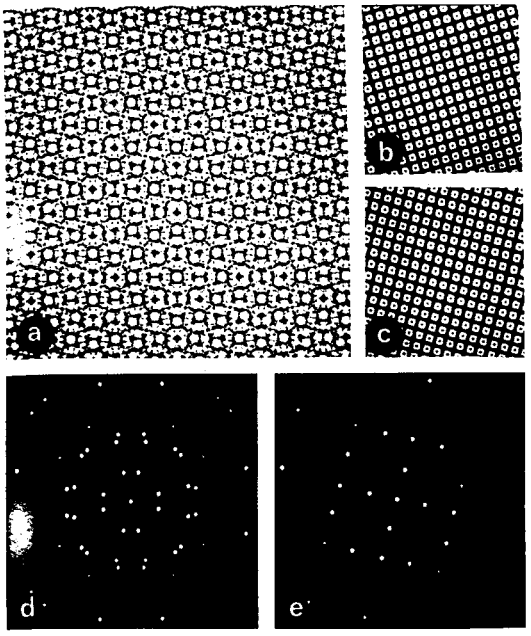


Fig. 2. Generation of a moiré pattern by superposition of two regular images. A rotational moiré pattern (a) is produced by superimposing two regular arrays (b,c) that have been rotated relative to one another. The shape of the subunits can be easily made out in a single layer, but is confused in the moiré pattern. The transform (d) of the superimposed layer contains spots from the transforms of each single layer, but the spots from each layer do not overlap. Thus the transform of a single layer (e) can be identified and used to reconstruct a single layer [in this case, (c)]. Reproduced with permission from Stewart (1986).

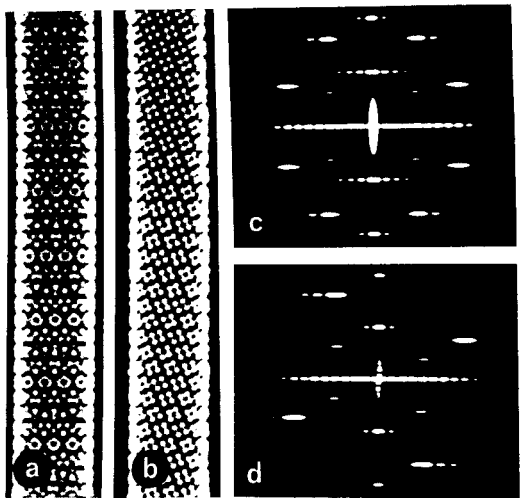


Fig. 3. Moiré pattern (a) produced by superposition of the patterns from the top and bottom of a helix. The transform of a helix (c) has elongated spots, but contributions from one side can be identified (d) and used to reconstruct a one-sided image (b) in which the location and substructure of the repeating units is clear. Reproduced with permission from Stewart (1986).

plane wave onto a cylinder. However, in contrast to the ideally infinite plane wave, a helical wave is limited and, moreover, must repeat an integral number of times in the circumference of the cylinder: that is to say, helical waves must have an integral rotational frequency, n. The other parameter that specifies a helical wave is the axial distance traversed for it to rotate azimuthally (that is, perpendicular to the helical axis) by one complete revolution: this is its pitch. Thus *each helical wave can be specified by three parameters: its radius, r; its rotational frequency, n; and its pitch, p.*

When analysing helical particles, it is generally more convenient to use cylindrical coordinates (see Fig. 6) rather than the more common Cartesian (x,y,z) ones. Thus, in real (image) space, the object density at any position is described in terms of its radius, r, its axial position along the direction of the helix axis, z, and its azimuthal rotation, $\phi$, about the helix axis. Similarly, in Fourier space, the position of a point in the transform is described in terms of its radius, R, its axial translation from the origin, Z, and its azimuth, $\Phi$. The same reciprocal relationships hold as in planar objects, so that $Z = 1/z$ and $R = 1/r$. The convention is that lower case is used for terms in real (image) space, whereas upper case is used for Fourier space.

The density distribution within a sheet of radius, r, will be the sum of all the possible helical waves that can be accommodated by the helical lattice. Like a plane lattice, the possible helical waves are severely restricted, and only those corresponding to the lattice and its "overtones" will contribute to the overall density. Consequently, only selected waves, having special values of n and p, will contribute to the object density. In this respect, therefore, an object with helical symmetry is analogous to a planar lattice in which only particular waves make a contribution to the density of a regular object. The density at any point in the helical object is the sum of all the helical waves at that point.

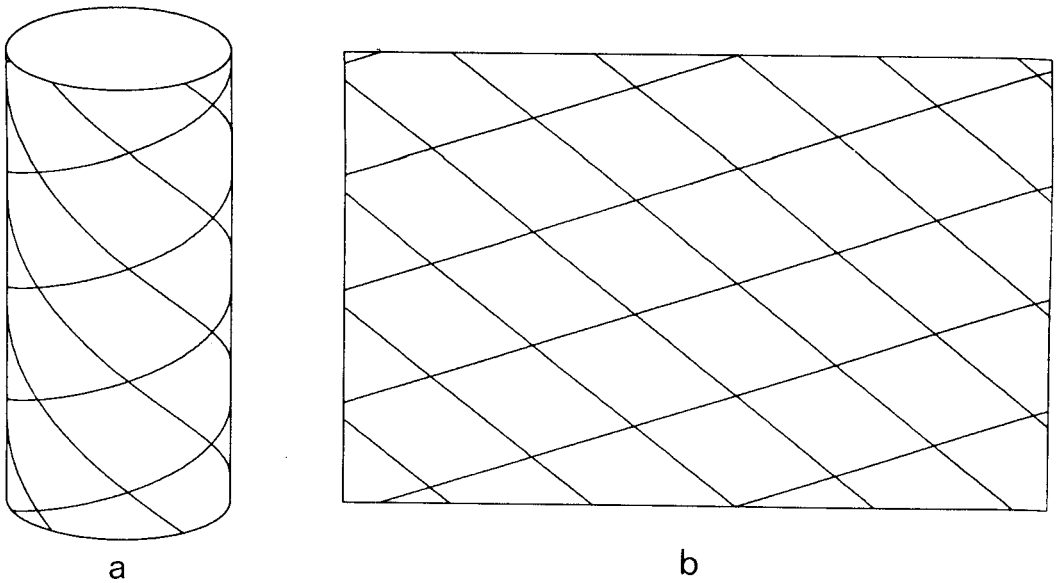


Fig. 4. Relation between a helical lattice (a) and a planar one (b). If the cylinder on which the helix is drawn is cut out and laid flat, it will give the pattern shown in (b) and, conversely, (b) rolled into a cylinder and joined along the vertical edges will give the helix (a). In contrast to the ideally infinite lattice used to describe planar arrays, the helical lattice has to repeat around the circumference of the cylinder and so is restricted to particular angular frequencies.

Because a helical object's density distribution can be conceived as a sum of helical waves, its Fourier transform will be a sum of the transforms of individual waves, in the same way as the Fourier transform of a planar array is the sum of the transforms of its constituent waves. Because the helical wave follows a curved surface, its Fourier transform is more complicated than that of a plane wave and, instead of being a pair of points, becomes elongated into a pair of lines, arranged symmetrically about the origin in the Fourier transform (Fig. 3). The lines are perpendicular to the direction of the helix axis (Z) and are spaced axially at multiples of the reciprocal of its pitch, p. These lines are generally referred to as "layer lines." Cochran et al. (1952) showed that the value of the Fourier transform, as a function of radius, R, along this line, is given by a Bessel function of order, n, multiplied by a phase term $\exp[in(\phi + \pi/2)]$. *Thus the magnitude of the transform of a helical wave is independent of azimuth, whereas the phase of the transform varies through n cycles of 0° to 360° for a rotation of 360° in the azimuth of the original helical wave.* This is a key result and forms the basis of the analysis and reconstruction of helical particles described below.

The Fourier transform of a helical structure therefore consists of a series of layer lines corresponding to the helical waves from which the object is constituted. The position of the layer lines and the distribution of intensity along them depends on the helical symmetry of the object and the structure of its subunits. In this context, there are some simple rules that govern the appearance of the Fourier transform of a helix. These rules become clear from a consideration of first, the transform of a continuous helix and second, the transform of a helix composed of a number of regularly spaced points (Cochran et al., 1952). As shown in Figure 7, the transform of a continuous helix of radius, r, and pitch, p, is a series of layer lines, perpendicular to the helical (Z) axis and spaced $l = 1/p$ apart. The first layer line corresponds to the basic helical wave, while the higher layer lines correspond to its overtones. As shown by Cochran et al. (1952), the value of the Fourier transform across a layer line is given by a Bessel function having the same order, n, as the layer line number, $l$. Bessel functions of

Fig. 5. Illustration of a helical wave. Density varies periodically in a cylindrical shell of radius r. Compare with the lattice shown in Figure 4. (The wave shown here corresponds to one of the directions present in the lattice in Figure 4.)

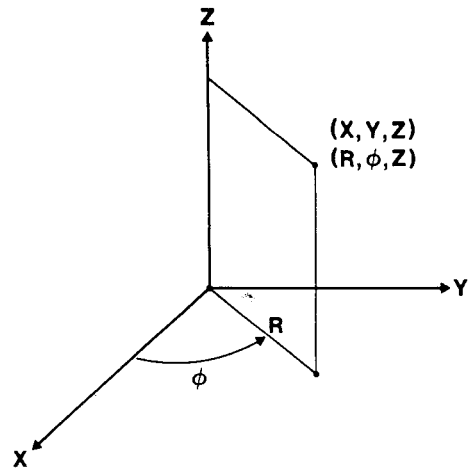


Fig. 6. Cylindrical coordinate system used to analyse helical particles and their Fourier transforms. A general point in the transform (X,Y,Z) is conveniently described in terms of its radius (R), azimuth ($\phi$), and axial position (Z).

rder n are denoted by $J_n$. Thus the zeroth ayer line (the equator of the transform) is given by a $J_0$ Bessel function, the first layer line by a $J_1$ Bessel function, the second layer line by a $J_2$ Bessel function, and so on. Figure 8 shows a plot of a number of Bessel functions of different order, n. With the exception of the $J_0$ function, they all have a similar shape, being initially zero, rising to a maximum before declining, and then oscillating to give a series of weaker subsidiary maxima. The $J_0$ Bessel function instead starts at its maximum value and then declines. The position of the first (primary) maximum of a Bessel function $J_n(x)$ occurs at higher values of x for increasing n and, as a first approximation, occurs at approximately x = n + 2. Table 1 lists the position of these maxima for Bessel functions of up to order 12. Because Bessel functions of increasing order have their primary maximum progressively further from the origin (which, in helical diffraction patterns corresponds to the meridian of the pattern), the transform of a continuous helix takes the form of a cross, centered on the origin (Fig. 7).

A discontinuous helix is produced by multiplying a continuous helix by an axial interference function with a repeat distance of a. If the helix were to be constructed from equally spaced points, its transform would take the form of a series of equally spaced lines perpendicular to the helix axis (see Fig. 7). The Fourier transform of a discontinuous helix is thus the transform of two functions multiplied together, which is equivalent to the convolution of their Fourier transforms [see Lipson and Lipson (1969) for a detailed discussion of this point]. This convolution means repeating the Fourier transform of a helix at each point of the transform that corresponds to the series of lines. Since the transform of the series of lines is simply a series of points spaced at 1/a along the Z axis, the composite transform will consist of a series of helical crosses (each containing layer lines spaced $l$ = 1/p apart) spaced by 1/a along the Z axis (see Fig. 7).

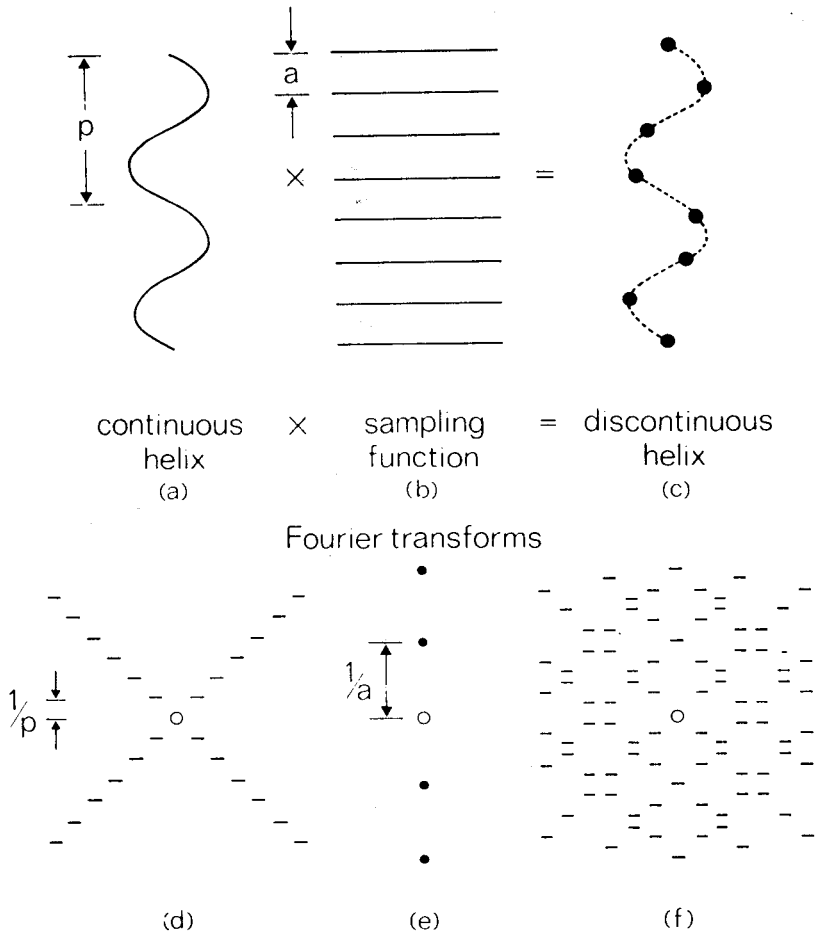


Fig. 7. Transform of continuous and discontinuous helix. A continuous helix in projection gives a cosine wave (a) of period, p, corresponding to the helical pitch. The transform (d) of this structure is a series of layer lines, spaced 1/p apart, which form a cross centred on the origin. A discontinous helix (c) is formed by multiplying a continuous helix by a sampling function (b) corresponding to lines spaced a apart. The transform of this sampling function (e) is a row of spots along the meridian spaced at 1/a. The transform of the discontinuous helix (f) is the convolution of the transforms of the continuous helix (d) and the sampling function (e) and so is a series of crosses centred on the spots corresponding to the sampling function.

The possible values of n and $l$ that are present in the Fourier transform of a helix are restricted, because only particular helical waves will make an identical contribution to all the subunits in the helical lattice. This is analogous to the restriction placed on two-dimensional waves in planar objects, although not quite as straightforward. It is, however, possible to derive a simple selection rule (Cochran et al., 1952; Klug et al., 1958) that predicts the possible combinations of n and $l$ for a particular helical symmetry. This selection rule states that if the structure has u units in t turns along a basic helix (that is, a helix that passes through all equivalent points in the lattice), then:

$$l = \mathrm{tn} + \mathrm{um}, \qquad (1)$$

where m is an integer that can be positive, negative, or zero. Moreover, this relationship gives rise to a regular lattice of points when n (rather than R) is plotted against $l$ or Z.

When using the selection rule, it is neces-

*TABLE*

| Bessel order |
|---|
| 1 |
| 2 |
| 3 |
| 4 |
| 5 |
| 6 |
| 7 |
| 8 |
| 9 |
| 10 |
| 11 |
| 12 |

sary to de
usual con
assign rig
orders. A
as one in
Fig. 6) ir
hand of a
mined by
or shadov

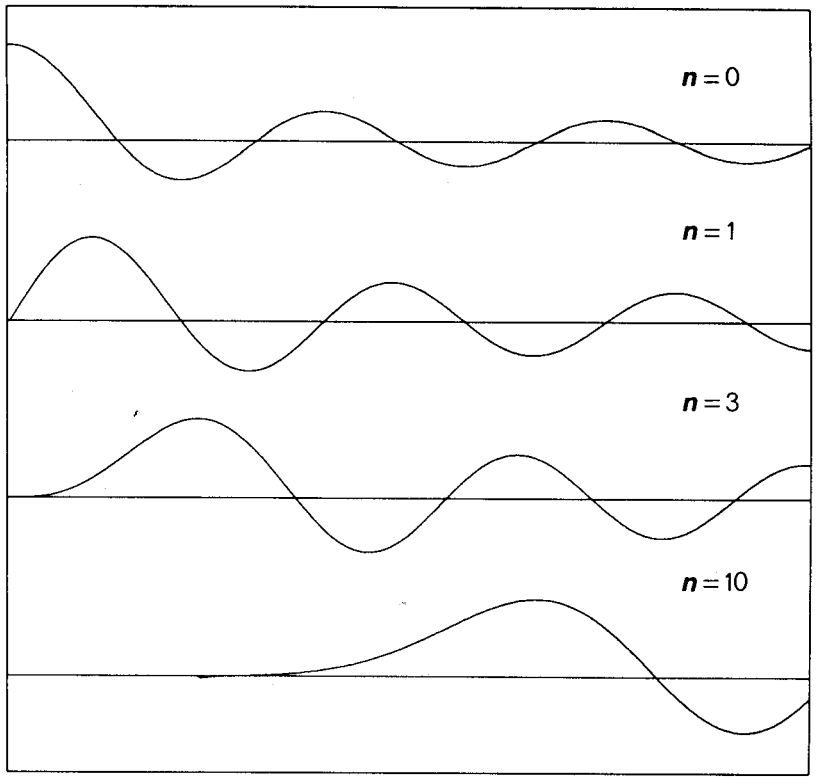


Fig. 8. Plot of Bessel functions of order 0, 1, 3, and 10.

*TABLE 1. Positions of Bessel function maxima*

| Bessel order | Value of $2\pi Rr$ for primary maximum |
|---|---|
| 1 | 1.8 |
| 2 | 3.1 |
| 3 | 4.2 |
| 4 | 5.3 |
| 5 | 6.4 |
| 6 | 7.5 |
| 7 | 8.6 |
| 8 | 9.7 |
| 9 | 10.7 |
| 10 | 11.8 |
| 11 | 12.8 |
| 12 | 13.9 |

sary to define the hand of helices, and the usual convention (Klug et al., 1958) is to assign right-handed helices positive Bessel orders. A right-handed helix is designated as one in which the azimuth (as defined in Fig. 6) increases with increasing z. The hand of a helical structure can be determined by tilting (for example, Finch, 1972) or shadowing (for example, Kensler and Stewart, 1983). Figure 9 illustrates the difference between right- and left-handed helices.

It is important to note that there can be Bessel functions of more than one order on any particular layer line (i.e., for any particular value of $l$ in the selection rule there are a range of values of n corresponding to the different values of m). Usually, at the comparatively modest resolutions encountered in electron microscopy, only a single Bessel function makes a major contribution to each layer line, but this is not always the case. This particular problem will be discussed in some detail later.

Sometimes there is not a single helix that runs through all equivalent positions. In this case there will be a number, k, of helices, related by a k-fold azimuthal rotation, that together will pass through all equivalent positions. (In other words, the structure will be composed of k helical strands). The effect of this situation is that only values of n that are multiples of k are

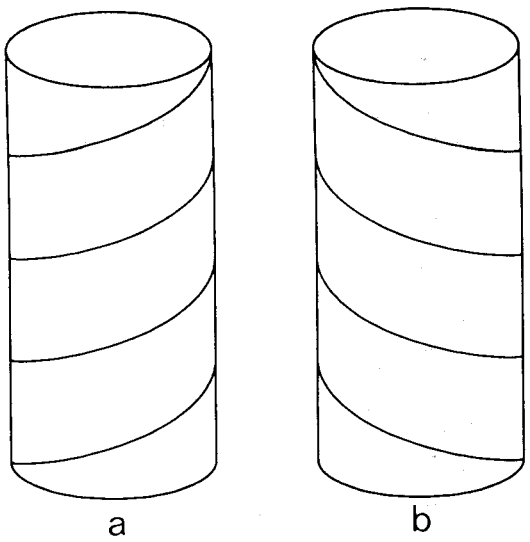


Fig. 9. Hand of helical structures. (a) shows right-handed helical tracks, whereas (b) shows left-handed tracks.

allowed in the selection rule. The use of the selection rule can be illustrated by an example. Consider a basic helix containing 7 units in 2 turns. The helical waves contributing to this structure are therefore defined as:

$$l = 2n + 7m.$$

If, as in bacteriophage T4, the structure is composed of six such helices (that is, k = 6), then n will be restricted to multiples of 6.

The value, F, of the Fourier transform along a layer line, $l$, (where the spacing of the first layer line corresponds to the axial repeat distance, c, of the helical object) can be easily calculated. If the particle density is conceived as a sum of helical waves, then the Fourier transform will be the sum of the transforms of these waves. Each (n,$l$) helical wave will give rise to a term of Bessel order n on layer line $l$, and so the value along a layer line is the sum of all the transforms of helical waves that contribute to the layer line. Thus:

$$F(\Phi,R,l) = \Sigma\, G_{n,l}(R)\exp[in(\Phi + \pi/2)]. \quad (2)$$

The value of each (n,$l$) term, $G_{n,l}(R)$, is related to the corresponding helical wave coefficient $g_{n,l}(r)$ by Fourier-Bessel transformation:

$$G_{n,l}(R) = \int g_{n,l}(r)J_n(2\pi Rr)2\,\pi r.dr \quad (3)$$

and

$$g_{n,l}(r) = \int G_{n,l}(R)J_n(2\pi Rr)2\pi R.dR \quad (4)$$

where $g_{n,l}(r)$ (which is a complex number) specifies the amplitude and phase of the helical wave of pitch c/$l$ and rotational frequency n, and $J_n(2\pi Rr)$ is a Bessel of order n and is defined by the integral

$$J_n(2\pi Rr) = 1/\pi \int_0^{\pi} (\cos(2\pi Rr\sin\theta) - n\theta)d\theta.$$

Bessel functions are easily evaluated by computer and are tabulated in standard textbooks such as Jahnke and Emde (1945).

Thus the value of the Fourier transform along a layer line is a sum of Bessel functions. The selection rule restricts the layer lines and Bessel orders that are found in the transform, so that only terms with values of n and $l$ that are consistent with the selection rule are non-zero.

## INDEXING HELICAL DIFFRACTION PATTERNS

Determining the helical symmetry parameters ("indexing") of a particle is perhaps the single most important step in its analysis and is a vital prerequisite for any subsequent processing. Unless the indexing is correct, all subsequent steps will lead to artefactual results that may be very difficult to recognise as such. Essentially, indexing the structure aims to associate all the layer lines present in the Fourier transform with a single selection rule and so recognise the parameters that specify the helical structure, namely: the number of subunits per turn and the number of helical tracks. This procedure is analogous to indexing a planar pattern, whereby one aims to find the underlying lattice and deduce its symmetry elements. And where one aims to determine a lattice and assign Miller indices for a planar pattern, for a helical pattern there is an analogous lattice assignment in terms of n and $l$. The problem of

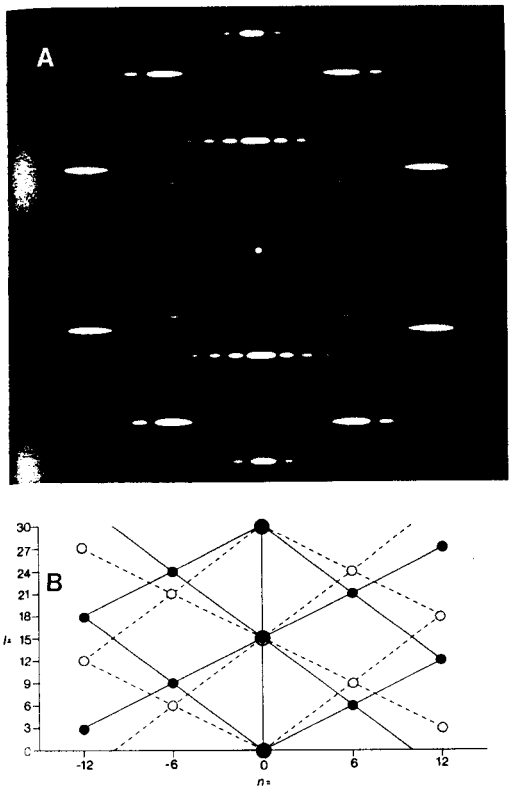


Fig. 10. The Fourier transform of a helix (a) gives a series of layer line reflections corresponding to its top and bottom that form two overlapping lattices. These can be most easily analysed in a (n,$l$) plot (b). This plot shows the lattice terms from the top (filled circles) and bottom (open circles) of the helix. Once the lattice has been identified, it can be used to deduce the helical symmetry, which in this case is six strands, each containing 15 subunits per turn.

indexing a helical diffraction pattern thus reduces to assigning values of n and $l$ to each layer line and thereby deducing the selection rule that specifies the object's symmetry. To do this, one first assigns an approximate lattice to the different layer line maxima in the pattern, as illustrated in Figure 10. One can then assign layer line numbers. These are often somewhat arbitrary, but one can usually draw an approximately equally spaced set of lines that contain all the maxima. One can then determine n from the radial position of each layer line maximum. This is most easily done if the structure is confined to a thin cylindrical surface so that all the material lies at a single radius, r. One then simply computes the value of the argument $2\pi Rr$ and compares it with values for different values of n. Table 1 lists values of the argument $2\pi Rr$ corresponding to the primary Bessel function maximum for values of n up to 12. Thus $2\pi Rr$ should be close to 1.8 for n = 1, 3.1 for n = 2, and so on. In practice, the material is usually spread over a number of radii, and so the distribution of intensity along the layer line does not follow exactly the shape of a Bessel function. But usually the intensity still has a pronounced peak close to that predicted, since terms from high and low radii tend to cancel to some extent. Flattening of the particle can also cause the radial position of the maximum to shift. If the particle simply collapses as, say, a result of radiation damage, then it will be indistinguishable from a native particle, since the projected density will not change. If, however, the particle is flattened by compressive forces (such as those from drying), then it will take on an elliptical cross section and appear to have an increased diameter. This effect can be difficult to detect without tilting the particle and, moreover, usually gives rise to a clearer optical diffraction pattern than seen with unflattened particles (Moody, 1967a). Since flattening due to compression increases the particle's apparent diameter, it will manifest itself in the transform by maxima appearing at a lower radius, R, along the layer lines than would be predicted. The magnitude of this effect depends on the degree of flattening, but calculations (for example, Moody, 1967a) indicate that it could reduce the apparent radius of the maximum by up to 20%.

It can sometimes be difficult to determine the radius at which most material in the structure is located, particularly when density appears superimposed as in an electron micrograph. One clue can come from the intensity distributions of any $J_0$ terms present. This is because, in addition to their central maxima, they usually show subsidiary maxima. The position of the first subsidiary maximum, which is a highly sensitive measure of the effective radius of the particle, occurs at a value of $2\pi Rr$ of about 3.8. Another clue to radii can come from fortuitous views down the helix axis that are sometimes observed with shorter particles, such as phage tails (Moody, 1967a) or tubes of bacterial surface layer proteins (Stewart and Murray, 1982; Stewart et al.,

1985a). However, even in these cases there is sometimes uncertainty about the precise value of n, although the number of possible alternatives is usually small. One method that is often effective in deciding between alternatives is to take advantage of the phase differences on opposite sides of a layer line. When the phase origin is located accurately on the helix axis, the phase of a particular Bessel term at a given radius passes through n cycles of 0° to 360° for an azimuthal rotation of the particle of 360° (see equation 2). Therefore it follows that for odd-order Bessel functions, the phase difference will be 180°, whereas for even-order Bessel terms it will be 0. Consequently, determining the phase difference on opposite halves of a layer line can often decide whether n is odd or even, and this test may be sufficient to enable a clear decision to be made between different symmetries. An example of this was seen in muscle thick filaments: *Limulus* (horseshoe crab) filaments were shown to be either three-, four- or five-stranded on the basis of the radial position of the prominent maxima on the first layer line, but since the phase difference between different sides was within a few degrees of zero, the structure had to be four-stranded, with the terms on the first layer line deriving from $J_4$ Bessel functions (Stewart et al., 1981). Similarly, both biochemical evidence and the position of the radial maxima indicated that frog muscle thick filaments were either three- or four-stranded, but a computed phase difference of close to 180° showed conclusively that these structures were three-stranded (Kensler and Stewart, 1983). A simple optical method for deciding whether terms have odd or even Bessel order has also been described (Aizawa and Maeda, 1980).

## SEPARATION OF CONTRIBUTIONS FROM THE TOP AND BOTTOM OF HELICES

Once the helical transform has been indexed, one can assign reflections to either the top or bottom of the structure and so reconstruct a view of one side (Klug and DeRosier, 1966), as illustrated in Figure 3. This view can often give a good idea of the arrangement and shape of subunits, particularly when most material is located over a narrow band of radii, as, for example, in muscle thick filaments (Stewart et al., 1981). But even when material is located over a range of radii, as, for example, in phage tails, simple one-sided views can often give a considerable insight into the arrangement of material. In the T4 phage tail, for example, such a filtered image showed clearly that there was material located primarily at two radii (Klug and DeRosier, 1966).

## THREE-DIMENSIONAL RECONSTRUCTION

Although one-sided filtered images of helical objects can often give a considerable insight into the arrangement and structure of subunits, a much more powerful method of investigating these features is to produce a three-dimensional reconstruction. This is often possible from a single view of a helical structure, because of the particular way in which the Fourier transform of a helical particle alters with azimuth. If the contribution on a particular layer line is made up from terms having only a single Bessel order, then, at a given radius, R, the amplitude of the transform (the sum of $G_{n,l}$ terms) will not change with azimuth, whereas its phase will change in a simple predictable way depending on the order n of the Bessel function (see equation 2). Specifically, the phase will pass through n cycles of 0° to 360° for every 360° of azimuthal rotation. Therefore, if the amplitude and phase are known for a particular azimuth of the particle, it is possible to predict the amplitude and phase for any other azimuth and thereby generate a three-dimensional transform of the particle. And once a three-dimensional transform has been obtained, a three-dimensional structure can be produced by Fourier inversion (although, in practice, this is more easily done by Fourier-Bessel transformation, as discussed below).

The density distribution seen in electron micrographs corresponds to a projection of the particle density in the direction of view (that is, parallel to the electron beam or perpendicular to the grid). A central theorem of Fourier transforms, the projection theorem (DeRosier and Klug, 1968), states that the Fourier transform of this projected density corresponds to a section through the three-dimensional transform of the object that contains the origin and is perpendicular to the direction of projection. If, as is usually the case, the helix axis is perpendicular to the direction of view, then the transform of the projected density will correspond to a section through the transform that contains the helical (Z) axis. Thus the Fou-

Fig. 11. Reconstructions of thick filaments from *Limulus* and scorpion muscle obtained after separating contributions from overlapping terms of different Bessel order on layer lines 0 to 9 inclusive. The two reconstructions on the left used all the data, whereas the equatorial data was omitted from those on the right. The reconstructions show bi-lobed projecting subunits that correspond to two myosin heads. Reproduced with permission from Stewart et al. (1985b).

rier transform of the projected structure seen in an electron micrograph gives the value of the three-dimensional transform at two azimuthal positions separated by 180°, which correspond to the back and front (or top and bottom) of the particle. If the helical symmetry is known, the manner in which phase varies with azimuth can be deduced for each layer line term. Consequently, a three-dimensional transform can be produced from the transform of each side, and this three-dimensional transform, in its turn, enables a three-dimensional density distribution to be produced by Fourier-Bessel inversion. If the particle density is formulated in terms of a sum of helical waves, $g_{n,l}$ terms can be computed from the corresponding $G_{n,l}$ term on each layer line, using equation 4. Once all the $g_{n,l}$ terms are known for the object, these can be used to resynthesise the density as a sum of helical waves.

Three-dimensional reconstructions of helical particles can be displayed in a number of ways. The overall envelope of the structure can be simulated either by making models out of sheets of balsa wood or transparent plastic, or by simulating the appearance of this sort of model using computer graphics methods (see Figs. 11 and 15). Sections through the structure are also useful and can be easily displayed as two-dimensional contour plots. The most useful types of section are perpendicular to the helix axis (so that the structure can be built up from a stack of successive sections) or cylindrical sections (at a constant radius, so that the density is built up from a number of coaxial cylindrical shells, rather like growth rings in a tree). The latter have the advantage that they are not influenced by the equatorial data (i.e., that from layer line zero), which is often less reliable than those from other layer lines. Figures 13 and 16 illustrate these sorts of section and how they can be used to investigate particular structural aspects. Other series of sections, such as a series containing the helix axis and differing in azimuth, or a stack of sections parallel to the helix axis, can be useful in some special applications.

## OVERLAPPING BESSEL TERMS

It is clear from the general formulation of the selection rule (equation 1) that there can be more than one Bessel order n on each layer line (there will generally be a different value of n for each value of m). Fortunately, at the comparatively low resolution (usually > 2 nm) that is generally present in electron micrographs of biological specimens, usually only one Bessel order contributes to a layer line; higher-order Bessel terms usually occur at higher resolutions (further out along the layer line) and are not present in the data analysed. However, in some instances, terms deriving from more than one Bessel order are present on a layer line. When this occurs, the Fourier transform cannot be analysed as simply, because the different Bessel terms will beat with one another, causing the amplitude at a particular radius to alter with azimuth. This behaviour comes about as a consequence of the way in which the phase of each $G_{n,l}$ term varies with azimuth (equation 2). Since each term goes through n cycles of 0° to 360° for 360° of azimuthal rotation of the object, the phase of higher-order terms will change more rapidly than that of lower-order ones. Therefore the phase difference between different $G_{n,l}$ terms will vary, thus altering the amplitude and phase of their sum. This behaviour is in marked contrast to the case of nonoverlapping Bessel terms and means that, when terms overlap, the three-dimensional transform cannot be deduced simply from a single view. Therefore, before these more complex objects can be analysed and

images reconstructed, it is necessary to separate overlapping terms along a layer line that derive from different Bessel orders. Except for the special case in which there are only two overlapping terms with one having an even Bessel order and the other having an odd order, more than one view of the particle is needed to separate the overlapping terms.

*Two overlapping Bessel terms, one odd and the other even*

Flagellar microtubules are an example of this problem, since layer line 1 [at Z = 1/(8 nm)] contains Bessel terms of order 5 and −8 (Amos and Klug, 1974). Layer line 2 has terms of order 10 and −3, but these are so widely separated that there is little overlap between them. The problem posed by the first layer line in microtubules is the simplest case of overlapping terms, because an azimuthal rotation of 180° of the object will change the phase of odd-order Bessel terms by 180° but will not alter the phase of even-order terms. The key to analysing this sort of structure is the realisation that the front of the particle is rotated by 180° relative to the back, and so the two halves of each layer line correspond to transforms of particles rotated by 180°. Thus, at any radius R on layer line 1 for flagellar microtubules, the value of the Fourier transform is given by:

$$F(\Phi) = G_5\exp(5i(\Phi+\pi/2)) + G_{-8}\exp(-8i(\Phi+\pi/2))$$

Taking one side as $\Phi = \pi/2$ and the other as $\Phi = -\pi/2$ gives:

$$F(-\pi/2) = G_5 + G_{-8}$$
$$F(\pi/2) = G_5 - G_{-8}$$

These two simultaneous equations can then be solved for $G_5$ and $G_{-8}$, which effectively separates the two terms of order 5 and −8. In this way, Amos and Klug (1974) were able to separate the $J_5$ and $J_{-8}$ terms of layer line 1 and so produce a three-dimensional reconstruction of flagellar microtubules to a resolution of 3 nm.

*Overlapping Bessel terms when particle azimuth can be determined directly*

Analysis of objects when there are two overlapping terms on a layer line that are both odd or both even are more complicated to analyse, because the rotation of 180° between top and bottom produces the same effect on each term (either shifting both by 180° if they are odd, or causing no change if they are even). Consequently, both sides of each layer line will be the same and so cannot be used to generate the simultaneous equations needed to separate the two $G_{n,l}$ terms. If there are more than two overlapping terms on a layer line, then it is clear that more than two simultaneous equations will be needed to separate them. In both these cases, therefore, more than a single azimuthal orientation of the original particle will be required.

Ideally, a series of different azimuthal views of a helical particle could be obtained by taking a tilt series of micrographs, with the tilt axis parallel to the helix axis (other orientations of the tilt axis could, in theory, be analysed, but would pose more difficulties); this has, in fact, been done in one instance (Stewart and Kensler, 1986—see below). However, obtaining data of this sort is technically demanding and can be seriously influenced by any flattening of the particle. An alternative strategy can be used when it is possible to determine the azimuthal orientation of each particle absolutely. If this is possible, then a number of micrographs of different particles, each having a different (but known) orientation, can be combined to give the necessary series of simultaneous equations needed to separate the overlapping Bessel terms. Such an analysis has been successfully employed to analyse thick filaments from arthropod muscles (Crowther et al., 1985; Stewart et al., 1985b). These filaments are four-stranded structures that have morphologic subunits separated by 14.5 nm axially and that repeat after 43.5 nm, so that each helix has a pitch of 12 × 14.5 = 174 nm. The helical selection rule is $4l = n + 12m$. Therefore, layer lines that are a multiple of 3 (that is, 0, 3, 6, 9 . . .) contain terms of order 0, +12, and −12, whereas other layer lines contain terms of order +4 and −8, or −4 and +8. Although an approximate one-sided image and three-dimensional reconstruction can be obtained by ignoring this overlap of terms (Stewart et al., 1981), a more correct and also more revealing view of the structure is obtained if they are separated. Fortunately, although the primary maximum of the $J_{-8}$ term on the first layer line overlaps with the secondary max-

imum of the $J_4$ term, the primary maximum of the $J_4$ term is not disturbed, and, since it is a strong feature of the structure, its phase (after being referred to a suitable origin) can be used to determine the azimuthal orientation of isolated particles unambiguously.

Although ideally only two different views would be needed to separate the overlapping $J_4$ and $J_8$ terms in the arthropod filaments' transforms, a more reliable result is obtained by using a larger number of views and determining the values most consistent with all of them. Crowther et al. (1985) devised a least squares method for achieving this separation, which is generally applicable to the problem of overlapping Bessel function terms. Thus, if there are k different Bessel terms of order $n_1$, $n_2$, $n_3$ . . . $n_k$ on a layer line, then the value of the Fourier transform at radius R and azimuth $\Phi$ will be

$$F(R,\Phi) = \Sigma\, G_k(R)\exp[n_k i(\Phi + \pi/2)]. \quad (5)$$

If there are v different views of the object, each associated with a different azimuthal orientation, $\phi_j$, there will be v different observed Fs giving v simultaneous equations in the unknowns $G_k(R)$. Provided the number of observations, v, is equal to or greater than the number of different Bessel orders, k, these equations will have a unique solution. In practice, each measured F will have an error associated with it, and so it is prudent to use substantially more views than the number of Bessel orders. Furthermore, the least squares solution of the simultaneous equations will be most reliable when the different views sample the possible orientations of the particle evenly. Thus, for example, if the particle is four-stranded, it will repeat every 90° azimuthally, and so views spanning orientations of 0° to 90° in approximately equal steps should be employed. If all the orientations used were similar (say, in the four-stranded example, clustered between 20° and 40°), then the least squares problem will be poorly posed, and the various $G_n(R)$ terms will not be determined very reliably. When a satisfactory data set has been obtained, each layer line is analysed over a range of radii, determining the values of the $G_n(R)$ terms from the values of the transform at each radial point. The procedure can often be simplified somewhat by noting that the value of Bessel functions is close to zero for $2\pi Rr$ less than $n - 2$, and so higher order terms can be omitted at lower radii. Fortunately, there is an internal check on this method. The manner in which the least squares problem is posed does not assume that the individual terms are derived from Bessel functions. One can therefore assess the likely reliability of a solution obtained in this way by inspecting the radial variation of the individual $G_n(R)$ terms. Poorly determined terms, in which the phase does not behave in approximately the expected manner, are probably best omitted from the reconstruction.

Arthropod muscle thick filaments are an example of a helical structure in which there are overlapping terms along layer lines, and they serve as an illustration of the results that can be obtained. Figure 11 shows reconstructions of *Limulus* and scorpion thick filaments (Stewart et al., 1985b); analogous results were obtained (Crowther et al., 1985) for tarantula. In all cases, the projecting morphological units are clearly bi-lobed; this appearance correlates well with the known presence of two myosin heads in each morphological unit. Cylindrical sections through the centre of the morphological units (Fig. 12) show the bi-lobed division of density particularly well. It seems more likely that the two heads in these units derive from different myosin molecules rather than from the same myosin molecule (Crowther et al., 1985; Stewart et al., 1985b), but the connectivity has been difficult to establish unequivocally, because this feature of the reconstruction is rather weak. The detailed appearance of the units depends on the equatorial data, which, as discussed below, are not as accurately determined as the other layer line data. The clear splitting of the morphological unit into two lobes was not apparent when the overlapping $J_4$ and $J_{-8}$ terms were not separated in a preliminary reconstruction (Stewart et al., 1981), although the overall outline of the morphological unit was essentially the same. The splitting into two lobes, which is critical for identifying the positions of the two myosin heads, was only seen when these terms were separated, and so our example underscores the importance of this technique when attempting to define fine detail.

### *More complicated examples*

With microtubules and Arthropod muscle thick filament examples described above,

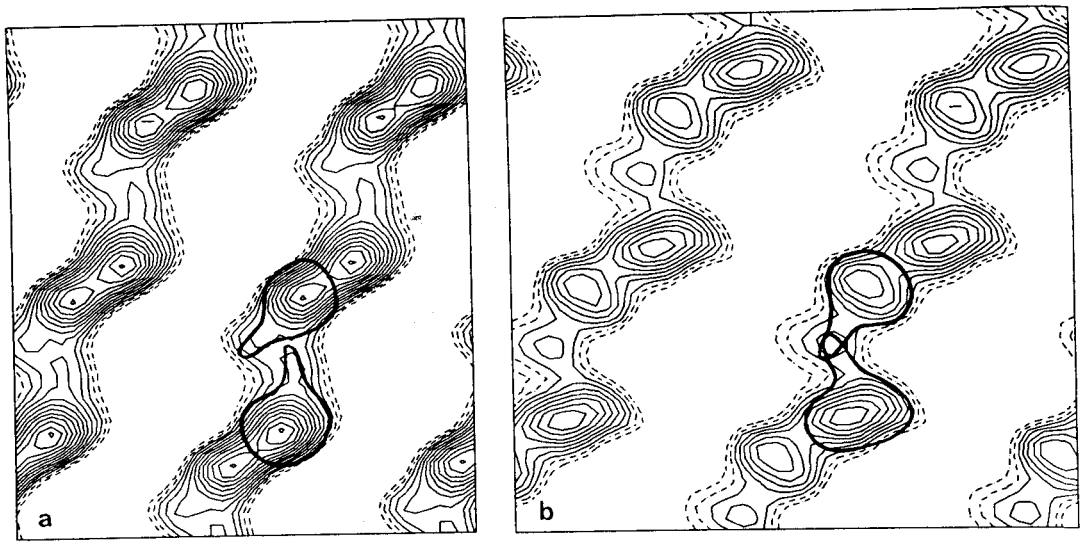


Fig. 12. Cylindrical sections of the scorpion (a) and *Limulus* (b) thick-filament reconstructions that show the division of the density of each projecting morphological unit into two lobes. The radius of these sections corresponds to the centre of mass of the morphological unit, and the probable outline of the myosin heads is shown on each. The data seem most consistent if the two heads in each morphological unit were derived from different myosin molecules. Reproduced with permission from Stewart et al. (1985b).

there were generally only two or three terms of different Bessel order overlapping on a layer line. Furthermore, because there were strong $J_4$ terms on the first and fourth layer lines that did not overlap with any other terms, the orientation of particles could be determined directly from inspection of their transforms. However, with other particles, azimuth sometimes cannot be determined directly from the transform, because there are no strong layer line peaks that derive from a single Bessel order term. It is then necessary to employ tilt series to separate the different $G_n(R)$ terms. An example is the thick filaments from frog skeletal muscle. These are three-stranded structures (Kensler and Stewart, 1983), but they have cylindrical rather than helical symmetry (Kensler and Stewart, 1986; Stewart and Kensler, 1986). This means that, on each layer line, there are terms of Bessel order 0, $\pm 3$, $\pm 6$, $\pm 9$ . . . , and so all the non-zero order terms overlap. Thus, for example, even the prominent inner maximum seen on the first layer line derives from overlapping $J_0$, $J_3$, and $J_{-3}$ terms. Consequently, the phase of the Fourier transform at a particular radius will not vary linearly with azimuth, but will follow an undulating path, as shown in Figure 13. However, because it is three-stranded, the structure will repeat after a rotation of 120°. Furthermore, one side will be 180° out of phase with the other. Consequently, the full 120° repeat can be spanned by an azimuthal rotation of only 60°, since the top half of the pattern (corresponding to the right-hand side of each layer line) will give the values of the Fourier transform from 0° to 60°, while the bottom half (the left-hand side of each layer line) will give the values of the transform corresponding to 60° to 120°. Therefore, a tilt series about the filament axis of 60° would sample all of the possible azimuthal orientations.

Although simple in concept, a tilt series of this nature was rather difficult to achieve in practice, because most particles examined had been flattened, either by drying or by radiation damage. The transform of a flattened particle does not vary in three dimensions in the same way as a native particle, and so cannot be used to decompose the overlapping terms. Fortunately, it was easy to detect flattened particles by measuring the azimuthal orientation required to change the phase of a prominent peak (in this case, the strong inner peak on the first layer line) to that observed initially for the corresponding peak on the other side of the

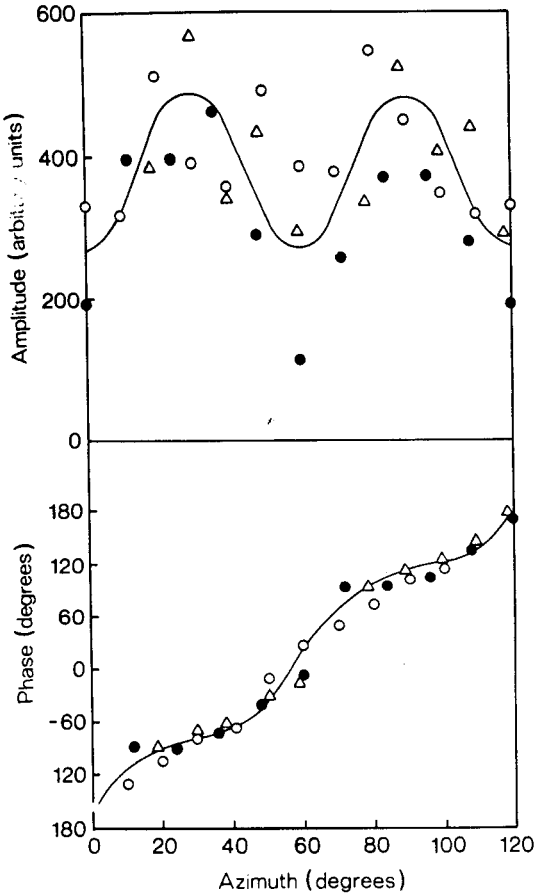


Fig. 13. Variation with particle azimuth of the amplitude and phase of the prominent inner maximum on the first layer line of transforms of frog thigh muscle thick filaments (data from three tilt series). The amplitude oscillates substantially, and the phase does not change linearly because of beating between terms of different Bessel order. Therefore reconstructions cannot be made from a single view, and, moreover, particle azimuth cannot be deduced a priori from the transform phase. Different symbols refer to different filaments. Reproduced with permission from Stewart and Kensler (1986), copyright Academic Press, 1986.

meridian. Ideally this should have been 60°, but it was increased in flattened particles. Thus, by recording tilt series over an 80° or 90° azimuthal range, it was possible to identify particles that had not been grossly flattened (a flattening of up to 20% was considered acceptable, as this could be compensated for with only marginal error by adjusting the value given the actual azimuth of the view). Tilt series from these particles could then be employed in subsequent processing to obtain the different $G_{n,l}(R)$ terms. It was found that particles simply negatively stained with uranyl acetate were invariably flattened too much to be employed in further processing, but some particles that had been pretreated with tannic acid (Kensler et al., 1985; Stewart and Kensler, 1986) were sufficiently well preserved. Three such particles were analysed and gave the $G_{n,l}(R)$ terms in Figure 14, which were used to produce the reconstruction in Figures 15 and 16. This shows projecting morphological subunits analogous to those seen in Arthropod muscle thick filaments, but they are perturbed axially, radially, and azimuthally from ideally helical positions; it is this perturbation that gives rise to the cylindrical symmetry of the filament (Stewart and Kensler, 1986). This is to say, the objects had translational symmetry and three-fold rotational symmetry, but these were not paired, as in a helix. Cylindrical symmetry is a lower form of symmetry, of which helical symmetry is a special case; it is discussed at length by Vainstein (1966).

## CORRECTION OF IMAGES

The discussion of helical objects thus far has assumed that the object is perfectly preserved, aligned perpendicular to the direction of view, and stained so as to perfectly reflect its structure. In practice, these criteria are seldom fully satisfied, and this will introduce some degree of error or artefact into any reconstruction obtained. However, it is often possible to at least partially correct for some of the shortcomings in the original micrographs and thereby obtain a more reliable result. Some corrections can also be made for errors introduced by the electron microscope imaging system.

### *Tilt corrections*

One often finds that the axis of a helical object is not exactly perpendicular to the optic axis of the electron microscope. This can come about either because the support film is not completely flat or because the object is sheared in a plane perpendicular to the support film. The magnitude of these effects is usually quite small, of the order of a few degrees, but nevertheless can introduce errors into the layer line data and result in an imprecise reconstruction. Figure 17 illustrates the effect on the Fourier transform of the helix axis being tilted. The

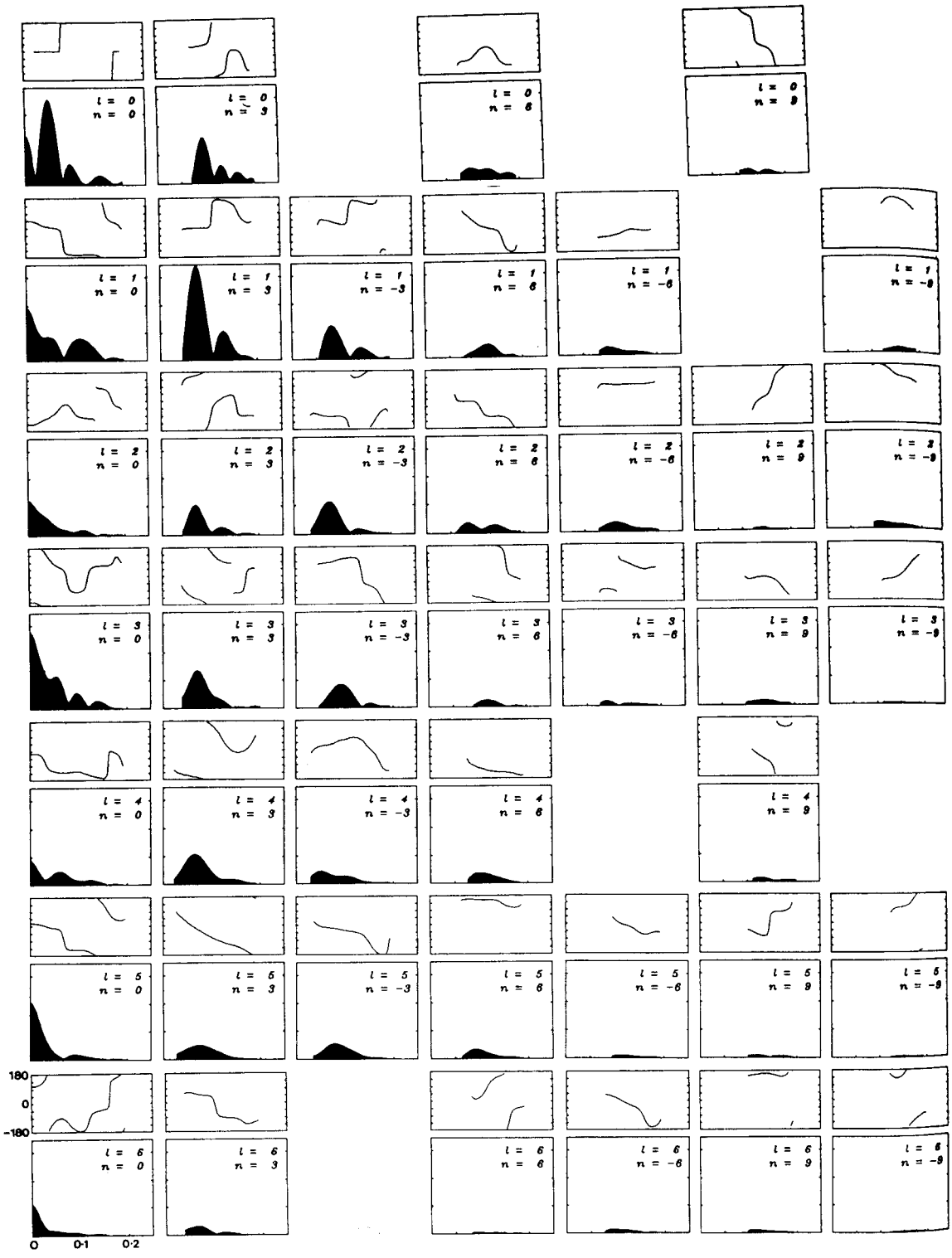


Fig. 14. Separated terms of different Bessel order obtained by least squares analysis of layer line data from three tilt series of frog muscle thick filaments. Reproduced with permission from Stewart and Kensler (1986), copyright Academic Press, 1986. For each combination of n and $l$, the phase is graphed in the upper box and amplitude in the lower box as a function of radius in Fourier space.

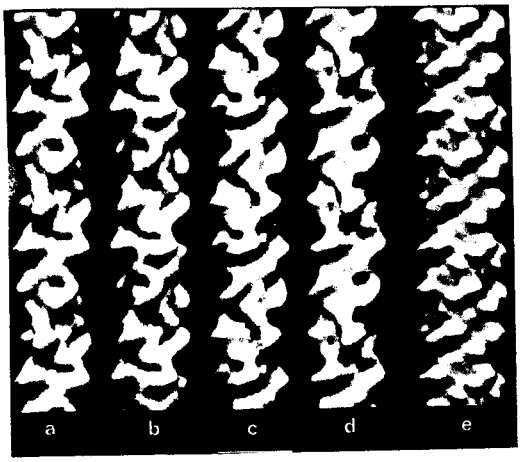


Fig. 15. Three-dimensional reconstruction of frog muscle thick filaments using the data from Figure 14. (a–d) are four views of the reconstruction rotated successively by 30°, whereas (e) is a reconstruction of scorpion muscle. The frog filament clearly has projecting morphological subunits analogous to those from Arthropods, but they are perturbed from the positions expected for a helical arrangement, and instead this structure has cylindrical symmetry. Reproduced with permission from Stewart and Kensler (1986), copyright Academic Press, 1986.

projection of the structure seen in the micrograph is now not perpendicular to the helix axis and so corresponds to a section through the three-dimensional Fourier transform that does not include the Z axis. This section will therefore not cut the successive radial anulii along a layer line on a diameter, but instead on a chord. Consequently, the phase of either side seen in the transform will be altered. In addition, a small portion of the layer line, corresponding to terms at low radius, will not be included at all. Fortunately, because the terms in the Fourier-Bessel integral used to generate the $g_{n,l}$ terms for a reconstruction (see equation 4) are weighted by their radius, R, this error has only a comparatively small influence on the final result. The radial position of the data along the layer

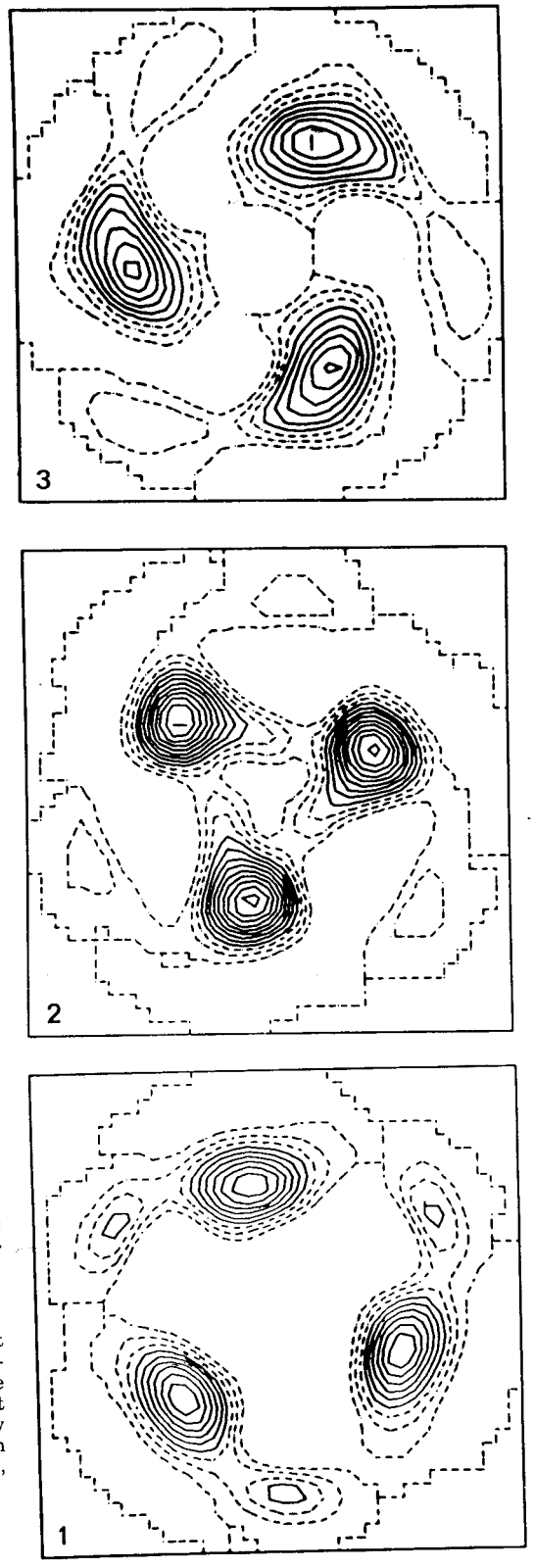


Fig. 16. Sections through the frog thick-filament reconstruction perpendicular to the axis at three successive levels of projecting morphological units. These sections show that the units on successive levels lie at different radii, in addition to being perturbed axially and azimuthally. Reproduced with permission from Stewart and Kensler (1986), copyright Academic Press, 1986.

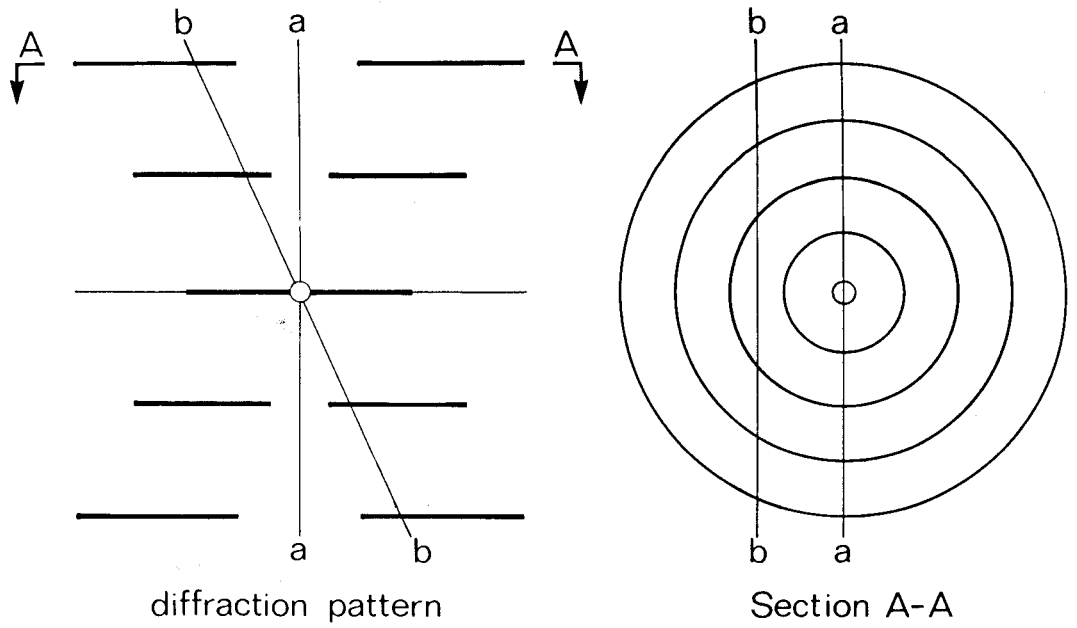


Fig. 17. Effect of particle tilt on the layer line data seen in a Fourier transform. A schematic diffraction pattern of layer lines is shown on the left. In an untilted object, the micrograph transform corresponds to a section (a-a) including the meridian. As can be seen in the cross section A-A, this section cuts successive annuli of the layer line along diameters. However, if the particle is tilted, the projected transform corresponds to section (b-b), which cuts successive annuli on chords. This effect alters the phase and radial scale of the projected transform. Because the sense of the phase change is different on opposite sides of a layer line, the phase gradient can be used to estimate the tilt and so correct the observed transform values.

line will also be slightly in error. High layer lines will have greater errors because the distance of the section from the axis will be greater; high-order Bessel terms will also have greater errors, since their phase changes more rapidly with azimuth. Errors will also be greater at lower radii.

The degree of tilt can be estimated from the phase errors on each layer line (see DeRosier and Moore, 1970) and, provided the errors are small, they can be adequately compensated for by introducing a phase shift, according to the radius and layer line number, and by altering the apparent radius of the term. If the particle is tilted by an angle $\alpha$, then on a layer line with apparent $Z = Z'$ and radius $R = R'$, the phase error $\Delta\theta$ is given by (DeRosier and Moore, 1970):

$$\Delta\theta = -2n \arctan(Z' \sin\alpha / R').$$

The actual value of the tilt angle, $\alpha$, is usually determined in conjunction with refinement of the phase origin (see below).

*Unbending*

One rarely finds micrographs in which helical objects are perfectly straight. They usually become curved to a greater or lesser extent as a result of forces arising from sample preparation (for example, drying in negatively stained material) or because of their inherent flexibility. As discussed in detail by Vainstein (1966), the effect of curvature is to spread layer lines axially to an extent that increases with radius in the Fourier transform. This has two effects: first, it makes weak data more difficult to detect above background noise; second, it means that if layer line amplitudes are obtained by interpolation along a line in the Fourier transform (as is usually done), they will be systematically underestimated at higher radii. Since the data in the Fourier-Bessel transformation used to generate the $g_{n,l}$ terms are weighted by the radius in the Fourier transform (equation 4), these effects can exert a considerable influence on the reconstruction. Consequently, particles used for reconstruction should be as straight

as possible. With many objects, one can eventually find sufficiently straight particles (that is, particles that are so slightly curved that the errors introduced are negligible) if a large number of fields is examined. However, some types of particle are so flexible that it becomes technically impossible to meet this criterion. This is particularly so for thin particles (which correspondingly have a low moment of inertia and high flexibility) with long helical pitches, such as actin and the paired helical filaments seen in Alzheimer's disease.

Egelman (1986) has devised an algorithm for correcting (or at least reducing) particle bending that is based on the normal engineering treatment of bending beams. The position of the helix axis is defined at a number of positions along the particle (using either a line printer grey-scale representation of the object, or, more conveniently, a raster graphics display). These data points are then fitted to a cubic spline function to define a smooth axial path and the data interpolated to compensate for bending along this path. (The method is in many ways analogous to the lattice correction schemes used to correct for irregularities in crystalline arrays—see, for example, Frank et al., 1978; Henderson et al., 1986; Saxton and Baumeister, 1982). This method has proved useful with tobacco mosaic virus (Egelman, 1986) and *rec*A protein/DNA aggregates (Egelman and Stasiak, 1986). It is, of course, limited to small degrees of curvature and by the accuracy to which the position of the helical axis can be defined. This latter consideration usually means that an improvement is obtained only out to a limiting radius in Fourier space (related to the accuracy to which the axis can be defined). This method may also be useful for helical particles preserved in vitreous ice, although it can only compensate for curvature in the plane of the film and not for any curvature in planes perpendicular to this. Autocorrelation methods for correcting distortions also appear promising (Chiu et al., 1986).

### *Corrections for microscope imaging conditions*

To a first approximation, the image of biological material seen in electron micrographs can be considered as arising by a combination of amplitude/aperture contrast and phase contrast arising from a weak phase object (see Erickson and Klug, 1971; Glaeser, 1985). Both mechanisms of image formation can be represented as multiplying the Fourier transform of the object by respective transfer functions (the phase contrast transfer function and the amplitude contrast transfer function). These contrast mechanisms produce different changes at different spatial frequencies, and so the resultant image is not exactly the same as the original object. Moreover, because these effects involve convolution in real space, they are often difficult to assess intuitively. With negatively stained material, amplitude/aperture contrast is strong at low spatial frequencies, whereas phase contrast is strong at higher frequencies. Therefore, provided the microscope is focused optimally, the image will not be greatly different from the original object density and can be interpreted with some confidence (Erickson and Klug, 1971). Work with tobacco mosaic virus has indicated that this is probably a valid procedure, at least to resolutions of the order of about 1/(2 nm), since differences between structures produced by electron microscopy and X-ray diffraction seemed to be due mainly to artefacts associated with negative staining (Unwin and Klug, 1974).

Helical objects (or in fact any bounded particle) viewed in vitreous ice may present problems, because here the image is formed mainly by phase contrast (reviewed by Stewart and Vigers, 1986). Consequently, low-frequency terms are substantially underestimated. Moreover, because such images are often recorded at rather large defocus values, the phase contrast transfer function may change relatively rapidly with position and so alter the relative weight of terms at different radii along a layer line as well as the relative weight of high and low layer lines. It therefore seems prudent to correct layer line data for the effect of phase contrast. This can be done by determining the degree of defocus from the position of the Thon rings (Thon, 1966) from a carbon support film, computing the value of the contrast transfer function for different spatial frequencies (see Erickson and Klug, 1971) and correcting the data accordingly. Because the contrast transfer function can sometimes be very small (resulting in large, and therefore unreliable, corrections), it would seem advisable to use data from a number of different defocus values. Failure to make this correction could result in changes in the weight of different helical

waves in the reconstruction. This error would be unlikely to affect the azimuthal and axial position of subunits greatly, but it could alter their shape and radial position. There are special problems with equatorial data from objects in vitreous ice; these are discussed below.

## COMPUTER PROCESSING OF HELICAL OBJECTS

Computer programmes for processing helical objects are freely available, and many of these have been described in some detail by DeRosier and Moore (1970). Figure 18 gives a flow chart of the sort of processing steps usually undertaken. In some respects the sequence is similar to that used for planar objects (Fig. 1): a large number of objects are scanned by optical diffraction to select only the best for processing; objects are then digitised for computer processing, areas are selected, and Fourier transforms are calculated. However, there are some special features that need to be considered for helical objects.

### *Position of particle boundary*

Because stain often falls off rapidly at the edge of a helical object (see Fig. 20), it is easy to underestimate the radial extent of the particle. Care is therefore needed when selecting the detailed area to process, if some high-radius information is not to be lost. When deciding where to choose the boundary, it is sometimes helpful to project the particle density axially. If in any doubt, it is probably better to use a large area for processing (with a consequent slight increase in the noise level), rather than risk losing high-radius data.

### *Digitising*

The theoretical discussion of helical transforms was based on a continuously varying object density and corresponding Fourier transform, whereas digital computing procedures use an object density and transform sampled at discrete intervals. There are some important consequences of this sampling. First, the object must be sufficiently finely sampled that significant information is not lost. Generally, it is necessary to sample the object density at a minimum of twice the frequency of the highest frequency term one wishes to retain (see section on sampling in Radermacher's article, this volume). Thus, to analyse the data to a resolution of 2 nm, sample raster points must be spaced on the original object to correspond to not greater than 1 nm (for a micrograph recorded at 30,000×, this would be a raster spacing of 0.03 mm). In practice, aliasing problems indicate that it is usually prudent to sample about twice as finely as indicated simply by resolution considerations, and even more finely if one wishes to interpolate the raw data onto a new raster (either for technical considerations or, for example, to correct for bending). DeRosier and Moore (1970) discuss these problems in some detail. Also, because of grain size and electron scattering, information on electron micrograph negatives is usually not well preserved below spacings (on the negative) of about 0.01 mm, and this may influence the actual choice of magnification at which images are recorded.

### *Effect of the shape function of the area selected for processing*

Helical objects are usually long and narrow, and so the area selected for Fourier transformation usually occupies only a small portion of the actual matrix of pixels transformed. (The rest are set to zero.) The edges of this "box" that encloses the particle makes a substantial contribution to the computed Fourier transform. It is particularly strong along the meridian and equator, but also influences the remainder of the transform to a greater or lesser extent. Figure 19 shows the transform of such a box function. It is clearly desirable to minimise the effect of this function. DeRosier and Moore (1970) suggested subtracting the average edge density of the box from all terms within it (which they called "floating" the image), thus minimising the difference between the object and the zeros surrounding it. This procedure certainly reduces the effect of the box function, but it can still be a substantial problem, particularly if one is trying to obtain accurate equatorial or meridional data.

The large contribution of the box function to the Fourier transform is a consequence of the well-known Gibbs phenomenon and is due to the sharpness of the edge of the box. It can therefore be reduced to virtually negligible proportions by making the transition between box and embedding zeros more gradual. This can be achieved by extending the edge density by a few pixels and gradually decreasing it as one moves further away from the box, so that it follows a

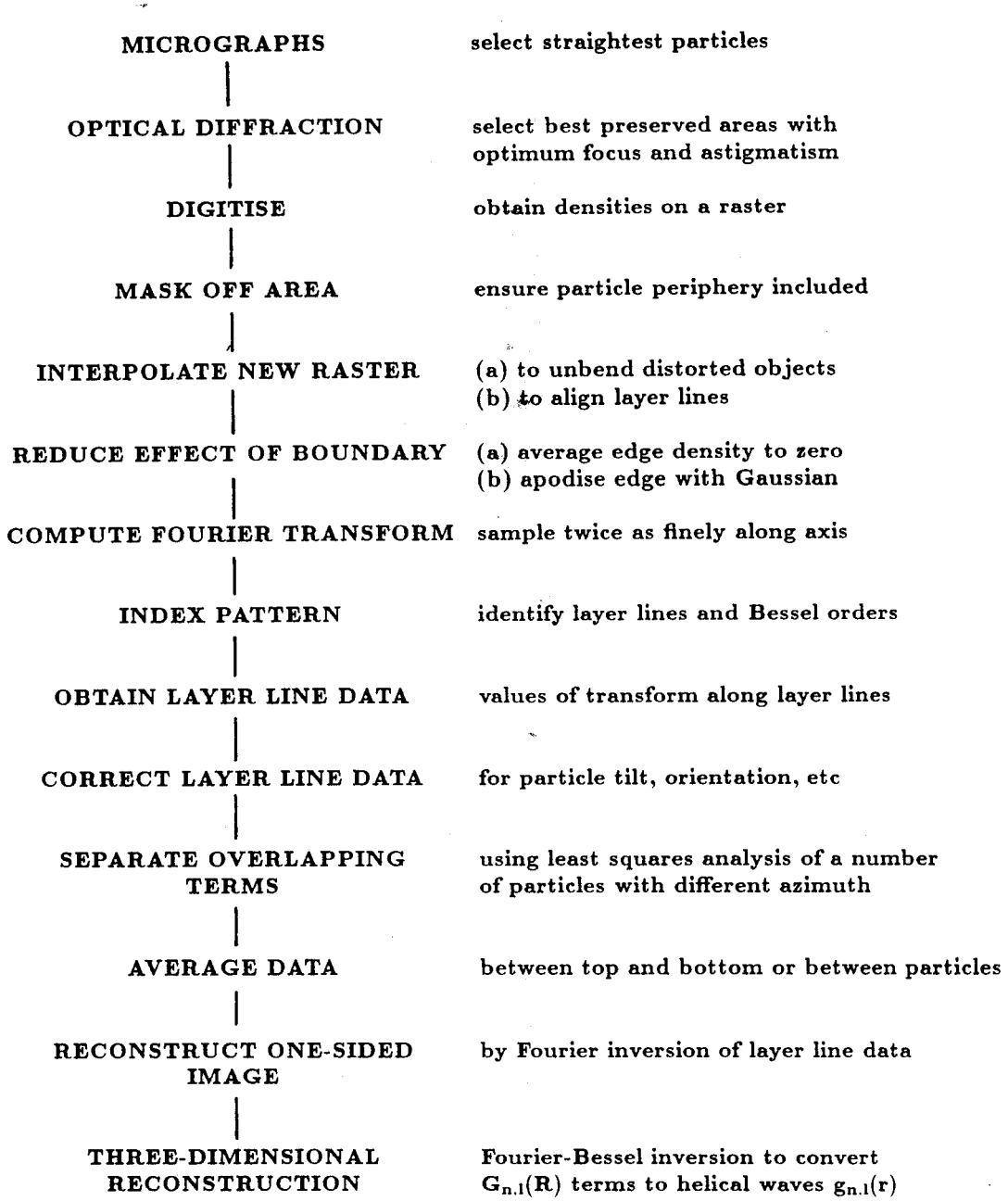


Fig. 18. Flow chart for the computer processing of helical particles.

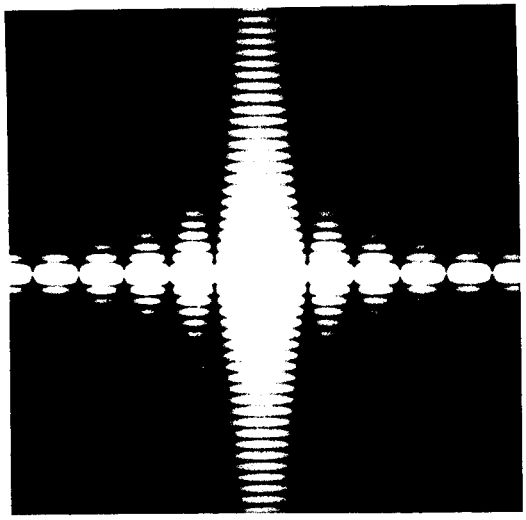

Fig. 19. Fourier transform of a rectangular box function. The transform has prominent "spikes" along equator and meridian and smaller contributions over the remainder. This effect can be greatly reduced by adjusting the average edge density of the particle to zero and apodising the edges of the box with a Gaussian or similar function.

Gaussian envelope (Stewart et al., 1981). This method is nothing more than a computer equivalent of the well-known optical technique of apodisation and is highly successful in reducing the effect of the box function.

*Obtaining layer line data*

It is also important to consider the effect of the digital nature of the transform on the reliability of layer line data obtained. Generally the value of the Fourier transform of a helical particle changes relatively slowly with radius along a layer line and so, provided sampling points are sufficiently finely spaced in this direction, values at a particular radial spacing can be safely determined by interpolation. Layer line data are usually extracted with a different radial sampling frequency to the transform by such interpolation. (This change in sampling may be because different particles have different magnifications or because it is required to perform a synthesis at a particular raster spacing.) However, it is important that the final sampling along the layer line must be finer than the reciprocal of the particle diameter because, as a consequence of convolution, when an image is reconstructed, a number of copies will be produced separated by the reciprocal of the spacing between points in Fourier space. Thus, if the spacing between sampling points in the transform is less than the inverse of the particle diameter, the reconstructed images will overlap, and the resultant density distribution will not reflect that of a single isolated particle.

A further problem can arise if the layer line does not lie along the sampling raster of the Fourier transform. This can come about because the layer line is not parallel to the transform sampling raster or, if it is parallel, because it lies between two lines of raster points. In either case, interpolation is not a very reliable procedure, because layer lines are usually fairly sharp in the axial direction. Thus, although the value of the transform may only vary slowly radially along a layer line, it varies rapidly in the axial (Z) direction (perpendicular to the layer line). This is particularly so if long, regular objects are studied. Although layer line data are often obtained by interpolation in such circumstances, they may be subject to considerable error, both in terms of relative weight of different layer lines and in terms of amplitude distribution along a layer line. These problems can be reduced substantially by interpolating a new density raster using the original image data (Stewart et al., 1981). Since the sampling raster in the Fourier transform is determined by the sampling raster in the object, a new object raster can be interpolated so that the layer lines are at least parallel to the transform sampling raster (by altering the orientation of the raster), and, if the layer lines are all evenly spaced axially (or at multiples of some axial spacing) they can also be made to correspond precisely to a line of sampling points in the transform (by adjusting the spacing between points in the image raster). This correction is particularly helpful when obtaining data for analysis by least squares to decompose overlapping Bessel terms (Stewart et al., 1985b; Stewart and Kensler, 1986) and results in a substantial reduction of the least squares residual.

*Determination of particle phase origin*

The phase relationships of helical diffraction theory hold only when the phase origin is located on the helix axis. If the phase origin is displaced radially by some dis-

tance, r, then all the terms along a layer line will undergo a phase shift of $2\pi Rr$. Although it is common practice to set the phase origin on the helix axis by eye when computing the Fourier transform, this positioning is seldom completely accurate and usually requires some adjustment. This problem is easily recognised by the presence of a phase gradient across the maxima on layer lines and is usually corrected, in conjunction with corrections for particle tilt, by observing the effect of making small changes in phase origin position and particle tilt on the layer line phase residuals. Ideally, the phase difference between points at the same radius but on different sides of the meridian will be either 0° or 180° (for even- and odd-order Bessel terms), and so, in this instance, the phase residual is defined as between the actual difference across the meridian and that predicted from the particle's helical symmetry. An effective way to make these corrections for tilt and phase origin position was described by DeRosier and Moore (1970) and involves finding (by trial and error) the combination of tilt and phase origin movement that minimises the amplitude-weighted phase divergence, Q, defined as:

$$Q = \Sigma \mid F \mid \mid \Delta\theta \mid )/\Sigma \mid F \mid ,$$

where $\Delta\theta$ is the difference between observed and predicted phases.

*Averaging data from different particles*

When averaging data from different particles, it is necessary to adjust the position of the phase origin along the helix axis and also to notionally rotate the particles so that they all have the same azimuthal orientation. Both these corrections are made by introducing appropriate phase shifts. In addition, it is usually necessary to determine particle polarity and adjust the radial scaling along layer lines. Ways of carrying out these adjustments have been discussed in some detail by Amos and Klug (1975) and usually involve the minimisation of some form of residual. After experimenting with a number of different types of residual (such as least-squares or residuals related to the Q residual above), they concluded that a residual of the type:

$$R(\Delta\phi,\Delta z) = \sqrt{(\Sigma \mid F \mid \Delta\theta^2/\Sigma \mid F \mid)}$$

was most appropriate, as it gave lower weight to the strong low-order terms that often contained little information about polarity. In this formulation, $\Delta\phi$ represents the azimuthal shift, $\Delta z$ the axial shift, and $\Delta\theta$ the phase error, which is given by:

$$\Delta\theta = \theta_2 - \theta_1 - n\Delta\phi + 2\pi Z\Delta z - k2\pi,$$

where $\theta_1$ and $\theta_2$ are the observed phases of the two particles and k is an integer, so that $\Delta\theta$ lies between $-\pi$ and $+\pi$. To determine orientation, minimum residuals are found for the particles in either orientation (that is, a second residual is determined for one particle turned upside down), and the lower of these corresponds to both particles having the same orientation. In some instances, such as muscle thick filaments (Stewart et al., 1981), orientation can be determined directly on the basis of defined characteristics of the particle.

In addition to positioning particles (by adjusting azimuth, axial translation, and orientation), it is also frequently necessary to adjust the radial scaling slightly. This is because different particles may shrink, stretch, or flatten to varying extents and also because magnification may vary slightly between micrographs. In adjusting this parameter, Amos and Klug (1975) found that a least squares residual between the two data sets was most useful. This is because the phase changes slowly across a peak (and so is a poor indicator of its position and thus radial scaling), whereas the amplitude (measured by the least squares residual) changes rapidly with position and so is much more sensitive to radial scaling. Thus the correct radial scaling can be determined by minimising the residual, S, defined as:

$$S(\Delta\phi,\Delta z) = \sqrt{(\Sigma \mid F_1 - F_2 \mid^2)},$$

where $F_1$ and $F_2$ are the values of the Fourier transforms after phase shifts appropriate for $\Delta\phi$ and $\Delta z$ have been applied to the second transform. Usually, the phase and least squares residuals are complementary and are used together to define the most appropriate parameters to fit one particle to another.

Generally one particle is chosen as reference and then the others fitted to it. To average data, differences in orientation are compensated for by applying phase shifts

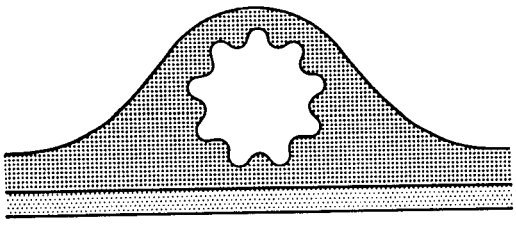

Fig. 20. Schematic representation of stain distribution around a negatively stained particle. Clearly the stain is not radially symmetric, and this introduces errors primarily on the equator.

and differences in radial scale by interpolating new values at the required intervals, so that all transforms correspond to one another. A similar series of steps is employed in preparing data for analysis by least squares to separate overlapping terms, although in this case the original orientations are not changed, and the fitting procedure is used only to adjust axial position, tilt, and radial scaling (Crowther et al., 1985; Stewart et al., 1985b; Stewart and Kensler, 1986).

## PROBLEMS AND INTERPRETATION

### *Equatorial data*

The formulation of helical diffraction given above assumes that the transform derives only from the object that is embedded in an infinite volume of zero (or, strictly, constant) density. This is clearly not strictly valid when considering negatively stained biological assemblies. Here the particle is embedded in a thin layer of stain, and the actual contrast in the image arises from the stain and not the object itself. Moreover, the stain layer is seldom of constant thickness but instead tends to follow roughly the contours of the particle, as illustrated in Figure 20. Consequently, the projected density recorded is not precisely that of the particle. This effect is most marked when considering the average cross section of the object, which gives rise to the equator in its Fourier transform. As shown in Figure 20, the amount of stain near the periphery of the object is generally less than would be expected if the helix were embedded in a uniformly thick stain layer; thus the object density inferred from the stain density will be too high in this region. Similarly, the object density will tend to be underestimated near the helix axis. For this reason, the equator computed from negatively stained electron micrographs is unlikely to represent that element of the structure very faithfully. Moreover, the stain envelope surrounding the particle may correlate with some structural features, particularly those that contribute most to the equator, and this can add further uncertainty to this aspect of the data (see Trus and Steven, 1984).

Errors in the equator can have a substantial influence on the reconstruction obtained, as this part of the Fourier transform gives rise to the $g_{0,0}$ helical wave that specifies the radial variation of density in the image. Errors in the equator will therefore result in the average density at different radii being incorrect. Consequently, the relative density of features at different radii may not be correct. Moreover, the undulating radial density variation so produced may result in contrast from other layer line terms (which is usually much less influenced by these errors) being superimposed on a sloping background; this can alter the shape and connectivity of different structural features. Problems with equatorial data can be even more involved when using tilt series (see, for example, Stewart and Kensler, 1986). Errors in the equatorial data can exert a considerable influence on the appearance of the reconstruction, and so some caution is usually required in making detailed interpretations of three-dimensional reconstructions of helical particles obtained in this way.

Obtaining reliable equatorial data from electron micrographs is usually very difficult. However, sometimes it is possible to obtain other estimates for the equator, and these can be used to obtain a more reliable reconstruction. End-on views of particles can sometimes be obtained [for example, in T4 phage tails (Moody, 1967a,b)], and these images can be used to obtain a measure of the radial density variation. Alternatively, X-ray diffraction data are sometimes available (as for such objects as tobacco mosaic virus and muscle filaments). In both these instances, however, there can be problems in scaling the equatorial data with that from the other layer lines.

Micrographs of helical objects embedded in ice do not suffer from the same problems with the equator, because, to a reasonable approximation, the ice layer is uniformly thick. There are, however, other problems with this sort of object, related mainly to its primarily phase nature. As a result, most

low-resolution terms are only weakly preserved in the image, and substantial correction is required before such data can be used with confidence (Stewart and Vigers, 1986). The problem is compounded by there being some uncertainty regarding the exact mechanisms of contrast generation at low resolutions in these images. When reconstructing electron micrographs of T4 bacteriophage tails in vitreous ice, Lepault and Leonard (1985) corrected only layer line data and used the native equator. Mandelkow and Mandelkow (1985) used an X-ray diffraction method to extend their low-resolution equatorial data for microtubules in ice. Although this method was quite successful in this instance, the success may have been because most of the contrast in microtubules was concentrated over a narrow band of radii. Trinick et al., (1986) used X-ray equatorial data combined with electron microscope layer line data when reconstructing actin filaments in ice.

Given the various problems associated with equatorial data in both negatively stained and frozen hydrated specimens, it seems prudent to always exercise considerable caution when interpreting features in reconstructions that can be influenced by errors present in this portion of the data. It is often useful to compute reconstructions with and without the equatorial data, to ascertain which features are independent of it and so are unlikely to be affected by errors of this nature. Reconstructions omitting the equator are also often useful in representing the local contrast in the specimen, which can be a helpful guide to resolving ambiguities of interpretation.

### *Material at different radii*

A number of problems of interpretation can arise when there is substantial material present at different radii in the object. Because the radial resolution is often only modest, density from features at different radii will often tend to merge, making the definition of boundaries difficult. This problem is compounded by errors due to the equatorial data. Moreover, it is important to realise that other errors in the reconstruction will not be uniformly spread over different radii. Layer line data are invariably truncated at high radii in the transform, and this will result in errors at low radii in the reconstruction. Moreover, since the integration used to generate the $g_{n,l}$ terms is R-weighted, errors at high radius in the transform will be accentuated. For these reasons, features near the helix axis should always be treated with considerable caution. Similarly, errors in particle tilt often mean that data near the meridian of the transform are not well determined, which results in errors, primarily at high radius in the reconstruction. Consequently, the most reliable region of the reconstruction is at intermediate radii.

### *Reliability of different aspects of reconstructions*

It is clear from the discussion above that some aspects of the structure are more likely to be faithfully preserved than others in three-dimensional reconstructions from electron micrographs. As in most Fourier-based image processing, the phase information in the layer line data is usually more reliable than the amplitude information. This is because the transform phase generally varies much less rapidly than amplitude and so is more reliably determined by interpolation. Phase information tends to influence position of features more than their weight, whereas the converse is true of amplitudes. Therefore, it is positional information that is generally most reliable in three-dimensional reconstructions. Consequently, positions of subunits are usually quite reliable. However, detailed shape information and relative weights of different features are more subject to error, both because of errors in the amplitude information and also because of the effect of errors in the equatorial data. It is therefore often difficult to decide on precise particle boundaries in reconstructions or on the connectivity between different structural features. An example of these problems can be seen with the reconstructions of Arthropod muscle thick filaments (Crowther et al., 1985; Stewart et al., 1985b) that were discussed earlier in the context of separating overlapping Bessel terms. As shown in Figures 11 and 12, the projecting morphological subunits in these reconstructions were bi-lobed, and this observation correlated with the presence of two myosin heads. Moreover, it was easily seen from these reconstructions that the two heads in each morphological unit were at slightly different radii. However, the actual connectivity between them was difficult to establish, as this was a weak feature and tended to be influenced by the

choice of equator employed. Thus, with *Limulus* and scorpion thick filaments, the appearance of this feature was not quite the same when the equator was omitted, included at full or half weight, or when a synthetic equator based on a cylindrical filament shaft surrounded by a halo of heads was employed. Also, it was not possible to define the exact outline of each head, because the data tended to merge substantially, although it was clear that the heads were elongate, pear-shaped objects and overlapped one another substantially.

Trachtenberg and DeRosier (1987) investigated the reliability of bacterial flagella reconstructions in considerable detail. They obtained reconstructions from a number of different particles and then computed the mean and variance of the density for each sampling point. In this way they were able to establish areas in which the density was significantly positive or negative using Student's t-test. Only the features of their reconstruction at intermediate radii were significant at the 95% level, and so, by using this method, they were able to make a decision about which aspects of their model should be treated with some caution. This statistical approach seems to offer great advantages when attempting to interpret three-dimensional reconstructions, and it would seem highly desirable to employ such methods when sufficient particles are available.

Another problem of interpretation is that it is not easy to place the data on an absolute scale, and so it is often not completely clear where particular features begin and end. If there is enough information available about the object, one can calculate the volume of different boundary contour values and choose one that gives a value consistent with the molecular weight of the subunits. However, this can only be an approximate guide, as negative stain, for example, rarely defines particle boundaries exactly.

Finally, three-dimensional reconstructions are density maps and not determinations of surfaces. Although one is usually primarily interested in surfaces, these are not obtained directly. Surface representations are generally obtained by presenting a single density contour, and the choice of this density contour is usually arbitrary to some extent. Often small changes in contour can alter the apparent shape of the particle, as can a sloping background, which is often produced by errors on the equator. Very careful examination of the data is often needed before attempting to define surfaces with any confidence.

## SOME APPLICATIONS

### *Virus particles*

Reconstructions have been obtained for a number of helical viruses, and these have proven useful in determining the general shape and arrangement of their capsid subunits. The most studied has been tobacco mosaic virus (Finch and Klug, 1971), which now also serves as an excellent test object, since high-resolution structural information is now available from X-ray diffraction on both the native virus (Namba and Stubbs, 1986) and its stacked disc aggregate (Champness et al., 1976). Studies of this system have also been useful in evaluating the effect of negative staining and radiation damage (Unwin, 1974). The tail of bacteriophage T4 has been studied in some detail. This structure undergoes a conformational change when infecting a bacterium. The helical tail of the bacteriophage contracts, and this forces its core into the bacterium rather like a hyperdermic needle. This injected core then serves as the route whereby the virus nucleic acid is introduced into the host. Amos and Klug (1975) and Smith et al. (1976) have examined the structure of the contracted and extended tail and thereby delineated the structural transition involved in the conformational change.

### *Actin filaments*

Actin is a major constituent of muscle thin filaments and is also widely dispersed in the cytoplasm of eukaryotic cells. It is often described as a double helix, but is more correctly analysed as a single helix with approximately 13 subunits in 6 turns. Individual filaments are quite flexible, and this has made it difficult to obtain straight specimens using negative staining, although actin in vitreous ice seems superior in this respect (Trinick et al., 1986). Reconstructions have been obtained from material in ice (Trinick et al., 1986) and also in negative stain from the paracrystals formed with magnesium or polylysine (O'Brien et al., 1983; Smith et al., 1983). The filaments in these paracrystals are much straighter than isolated ones, but there may be problems from superposition and intercalation (Egelman, 1985). Reconstructions generally

show that the actin subunits are bi-lobed, with the lobes located at different radii. There is some controversy about connectivity, and it is not completely certain whether the lobes in a subunit are connected along the long-pitch or short-pitch helices. This problem has proven difficult to resolve, because it depends primarily on determining the relative intensities of the first and sixth layer lines. The usual problems in determining such values accurately in computed transforms are compounded here by torsional disorder (Egelman et al., 1983), but the balance of opinion probably favours connectivity along the short-pitch helices (Egelman, 1985). In muscle, actin is associated with tropomyosin and troponin. (These two proteins constitute the calcium-sensitive regulatory switch in skeletal muscle.) Tropomyosin is a rod-shaped molecule that lies in the grooves of the actin helix and can be seen in reconstructions (Milligan and Flicker, 1987; O'Brien et al., 1983; Spudich et al., 1972; Wakabayashi et al., 1975). X-ray diffraction indicates that tropomyosin moves in the actin groove in response to changes in calcium ion concentration (this movement is mediated by conformational changes in troponin), and reconstructions of thin filaments in either active or passive conformations are consistent with this model (O'Brien et al., 1983; Wakabayashi et al., 1975).

### *Decorated actin filaments*

Contraction in muscle and many other systems is brought about by the interaction of myosin and actin. Myosin is a rod-shaped molecule with two globular heads that interact with actin. Proteolytic myosin fragments corresponding to the heads also bind to actin in the absence of ATP and form characteristic arrowheads. Decorated actin filaments have been studied extensively to define the shape of myosin heads and the interaction geometry (Amos, 1985; Amos et al., 1982b; Milligan and Flicker, 1987; Moore et al., 1971; Taylor and Amos, 1981; Wakabayashi and Toyoshima, 1981). These have proven difficult objects, however, because material is present over a wide range of radii, and, since the structure is rather open, it is easily distorted. It has therefore been rather difficult to decide on exact boundaries between particles, although clearly the actin is located near the helix axis, whereas myosin is located at intermediate and high radii. The interaction geometry has suggested that tropomyosin might regulate skeletal muscle contraction by a "steric blocking" mechanism. The myosin heads in these reconstructions are also clearly curved and attach at an angle to the actin helix. Decorated actin has also been used to locate myosin light chains in the heads by obtaining reconstructions with and without light chains present. The difference between these two reconstructions indicated that the light chains were located at high radius and so near the junction of the heads with the tail in the myosin molecule (Vibert and Craig, 1982). The myosin ATP-ase has also been located in a similar way by labelling the site with avadin (Tokunaga et al., 1987).

### *Myosin-containing filaments*

A number of muscle thick (myosin-containing) filaments have been investigated. The arrangement of myosin heads on the surface of a number of Arthropod thick filaments (Crowther et al., 1985; Stewart et al., 1981, 1985b) has been established and has been further shown to be remarkably similar, even though the filaments themselves have different diameters. The arrangement of myosin heads has also been established in scallop (Vibert and Craig, 1983), *Mytilus* (Castellani et al., 1983) and frog (Kensler and Stewart, 1983, 1986) filaments. Vertebrate thick filaments are somewhat different from invertebrate in that they have cylindrical rather than helical symmetry (Kensler and Stewart, 1986; Stewart and Kensler, 1986). This made reconstructions more difficult to obtain, although Stewart and Kensler (1986) have obtained one for the frog at modest resolution, using tilt series to decompose overlapping terms of different Bessel order. This reconstruction has shown that the heads are perturbed axially, azimuthally, and radially from the positions expected for an ideal helix, possibly as a consequence of the manner in which the myosin tails pack in the filament shaft. Moreover, these reconstructions indicated the position of accessory proteins and a marked positive-staining pattern in the filament shaft.

### *Microtubules*

Flagellar microtubles have been analysed in some detail and a three-dimensional reconstruction of flagellar A-tubules gener-

ated that shows the general position of the tubulin monomers in the structure (Amos and Klug, 1974). Generally in this structure the α- and β-tubulins are thought to be arranged alternately along each of the three-start genetic helices of the structure. Microtubules reassembled in vitro from cytoplasmic tubulin lack this symmetry. Mandelkow et al. (1986) suggest that alternate genetic helices contain either all α- or all β-tubulin, so that these structures have a helical dislocation or seam along one side, thus resembling the C-shaped flagellar B-tubule. Cytoplasmic microtubules have also been investigated in vitreous ice and shown to have a very long-pitch supertwist (Mandelkow and Mandelkow, 1985). The arrangement of high-molecular-weight accessory proteins ("MAPS") has also been investigated (Amos, 1977), and these proteins appear to form a superlattice of the A-tubule type microtubule lattice.

### *Bacterial flagella*

Bacterial flagella are composed of a single protein, flagellin, but they are polymorphic and assume several different structural conformations, most of which are curved. Two of these conformations are related to the physiologic "swimming" and "tumbling" states, but the entire series can be viewed as a series of mixtures of two basic structural states (Calladine, 1978). The structure of the most common straight form of flagella, which represents one of these states, can be described by a selection rule $l = 15m + 82m$ (Finch and Klug, 1972; O'Brien and Bennett, 1972), which indicates just over 11 subunits in 2 turns. Three-dimensional reconstructions of these straight flagella (Shirakihara and Wakabayashi, 1979; Trachtenberg and DeRosier, 1987) show a range of different interactions between subunits at different radii in the structure, which may be related to the observed polymorphism. These reconstructions also give some idea of the structure of the subunit, although it is difficult to make an unequivocal assignment of connectivity between different domains Shirakihara and Wakabayashi (1979) reconstructed negatively stained material and suggested that there were four domains, whereas Trachtenberg and DeRosier (1987) found only three significant domains when reconstructing material in amorphous ice. However, there was a remarkable correspondence between many aspects of these two models, and the multidomain structure deduced for the subunit may impart the flexibility necessary for the structural transitions involved in generating the various polymorphic configurations. Another straight flagella configuration has also been examined and is thought to correspond to the other basic state from which the curved polymorphs are derived (Kamiya et al., 1979). This second straight form has an opposite helical hand to the first type, but its exact helical structure does not seem to have been established unequivocally. Trachtenberg et al. (1987) have also studied more complex flagella from *Rhizobium lupini* H13-3 and have demonstrated in this case that there is a pairing of subunits to give three prominent helical strands on the exterior of the filament that seem to be associated with its greater rigidity and more brittle nature. The hooks that link flagella to the "motor" in the bacterial plasma membrane have also been investigated and have helical parameters remarkably similar to those of flagella (Wagenknecht et al., 1981). Three-dimensional reconstructions of hooks show prominent six-start helical grooves at medium to high radius; this feature may be important in conferring flexibility. Flagella hooks are polymorphic and seem able to assume a range of conformations analogous to those in flagella (Kato et al., 1984).

### *Other helical objects*

A range of other helical objects have been examined. Gastropod hemocyanin (Mellema and Klug, 1972) showed the subunits arranged around the wall of a hollow cylinder, while the general outline of molecules such as catalase (Kiselev et al., 1968), glutamine synthetase (Frey et al., 1975), and nucleosomes (Klug et al., 1980) have been determined from helical aggregates. Bacterial pili (Steven et al., 1986) have been investigated in some detail and seem to have different surface lattices, depending on the organism from which they were obtained. Most, but not all, of the pili structures appear to have a central hole, but there does not appear to be any systematic relationship between the different structures analogous, for example, to that seen for bacterial flagella. A rather open and flexible helical structure, which seems to be based on two filaments winding around each other, is the sort of paired helical filament seen in Alz-

heimer's disease (Wischik et al., 1985) and in aggregates of X protein from skeletal muscle (Bennett et al., 1985). Reconstructions have also been obtained of the complex helical filaments formed from sickle-cell hemoglobin (Carragher et al., 1988; Garrell et al., 1979). Electron microscopy and image processing have also given insights into aggregates of helical molecules such as actin in acrosomal processes (DeRosier et al., 1977), paramyosin in the core of some molluscan muscle thick filaments (Elliott and Bennett, 1984), crystalline tubes of myosin subfragment-2 (Quinlan and Stewart, 1987), and *rec*A protein-DNA complexes (Egelman and Stasiak, 1986).

## CONCLUSIONS

Helical structures are widespread in biological systems, such as viruses, and subcellular assemblies, such as cytoplasmic filaments, flagella, and pili. These can often be ideal objects for analysis to moderate resolution (about 2 nm) by electron microscopy and image processing because of the ease with which three-dimensional models can, in many instances, be generated from a single view. Central to any form of analysis of these objects is the decomposition of their density distribution into helical waves and the consequent expression of their Fourier transform in terms of sums of Bessel function terms. Provided the diffraction pattern can be correctly indexed, these terms can be evaluated quantitatively and reliable reconstructions can be produced. This is most easily done when terms of different order do not overlap along layer lines, but, if they do, then objective methods, based on least squares analysis of a number of different views of the particle, are available to separate overlapping terms.

Although analysis of helical particle can sometimes involve considerable effort, the results obtained can often be spectacular, and insights into the structure can be obtained that cannot be achieved by simple inspection. These methods are, like the majority of image processing methods, most powerful in detecting positions and orientations of subunits and are often less precise regarding particle outlines and relative densities. This is particularly so when material is distributed over a substantial range of radii and so likely to be influenced by errors in the equatorial data. Notwithstanding these difficulties, image analysis of helical particles has proved a powerful tool in the analysis of these structures and in yielding a wealth of quantitative information about the structure, function, and assembly of many biological systems.

## ACKNOWLEDGMENTS

I am indebted to my colleagues in Cambridge, in particular Linda Amos, Wah Chiu, Richard Henderson, Hugh Huxley, and Aaron Klug, for their assistance and many helpful comments on the manuscript.

## REFERENCES

Aebi, U., Fowler, W.E., Isenberg, G., Pollard, T.D., and Smith, P.R. (1981) Crystalline actin sheets: Their structure and polymorphism. J. Cell Biol., 91:340–351.

Aebi, U., Fowler, W.E. Buhle, E.L., and Smith, P.R. (1984) Electron microscopy and image processing applied to the study of protein structure and protein-protein interactions. J. Ultrastruct. Res., 88:143–176.

Aizawa, S.-I., and Maeda, Y. (1980) A new method for determining the parity in optical diffraction patterns from structures with helical symmetry. J. Mol. Biol., 137:437–442.

Amos, L.A. (1974) Image analysis of macromolecular structures. J. Microsc., 100:143–152.

Amos, L.A. (1977) Arrangement of high molecular weight associated proteins on purified mammalian brain microtubules. J. Cell Biol., 72:642–654.

Amos, L.A. (1985) Structure of muscle filaments studied by electron microscopy. Annu. Rev. Biophys. Biophys. Chem., 14:291–313.

Amos, L.A., and Klug, A. (1974) The arrangement of subunits in flagellar microtubules. J. Cell Sci., 14: 523–549.

Amos, L.A., and Klug, A. (1975) Three-dimensional reconstruction of the contractile tail of T-4 bacteriophage. J. Mol. Biol., 99:51–73.

Amos, L.A., Henderson, R., and Unwin, P.N.T. (1982a) Three-dimensional structure determination by electron microscopy of 2-dimensional crystals. Prog. Biophys. Mol. Biol., 39:183–231.

Amos, L.A., Huxley, H.E., Holmes, K.C., Goody, R.S., and Taylor, K.A. (1982b) Structural evidence that myosin heads may interact with two sites on F-actin. Nature, 299:467–469.

Bennett, P.M., Starr, R., Elliott, A., and Offer, G. (1985) The structure of C-protein and X-protein molecules and a polymer of X-protein. J. Mol. Biol., 184:297–309.

Brisson, A., and Unwin, P.N.T. Tubular crystals of acetylcholine receptors. (1984) J. Cell Biol., 99:1202–1211.

Buhle, E.L., Knox, B.E., Serpersu, E., and Aebi, U. (1983) Structure of the Ca ATPase revealed by electron microscopy and image processing of ordered arrays. J. Ultrastruct. Res., 85:186–203.

Calladine, C.R. (1978) Change in waveform in bacterial flagella: Role of mechanics at the molecular level. J. Mol. Biol., 118:457–479.

Carragher, B., Bluemke, D.A., Gabriel, B., Potel, M.J., and Josephs, R. (1988) Structural analysis of polymers of sickel cell hemoglobin. J. Mol. Biol., 199:315–331.

Caspar, D.L.D., and Klug, A. (1962) Physical principles

in the construction of regular viruses. Cold Spring Harbor Symp. Quant. Biol., 27:1–24.
Castellani, L., and Hardwicke, P.M.D. (1983) Crystalline structure of sarcoplasmic reticulum from scallop. J. Cell Biol., 97:557–561.
Castellani, L., Vibert, P., and Cohen, C. (1983) Structure of myosin/paramyosin filaments from a molluscan muscle. J. Mol. Biol., 167:853–872.
Champness, J.N., Bloomer, A.C., Bricogne, G., Butler, P.J.G., and Klug, A. (1976) The structure of the protein disc of tobacco mosaic virus to 5 A resolution. Nature, 259:20–24.
Chiu, W., Schmid, M.F., and Jeng, T.-W. (1986) Computer processing of high resolution images of periodic specimens. In: Proceedings 44th EMSA Meeting. G.W. Bailey, (ed). San Francisco Press, San Francisco, pp. 2–5.
Cochran, W., Crick, F.H.C., and Vand, V. (1952) The structure of synthetic polypeptides. I. The Fourier transform of atoms on a helix. Acta Crystallogr., 5:581–586.
Cooley, J.W., and Tookey, J.W. (1965) An algorithm for the machine calculation of the complex Fourier series. Math. Comput., 19:297–301.
Crowther, R.A., Padron, R., and Craig, R. (1985) Arrangement of the heads of myosin in relaxed thick filaments from tarantula muscle. J. Mol. Biol., 184: 429–439.
DeRosier, D.J., and Klug, A. (1968) Reconstruction of three-dimensional structures from electron micrographs. Nature, 217:130–134.
DeRosier, D.J., and Moore, P.B. (1970) Reconstruction of three-dimensional images from electron micrographs of structures with helical symmetry. J. Mol. Biol., 52:355–369.
DeRosier, D.J., Mandelkow, E., Silliman, A., Tilney, L.G., and Kane, R. (1977) The structure of actin-containing filaments from two types of non-muscle cells. J. Mol. Biol., 113:679–695.
Egelman, E.H. (1985) The structure of F-actin. J. Muscle Res. Cell Motil., 6:129–151.
Egelman, E.H. (1986) An algorithm for straightening images of curved filamentous structures. Utramicroscopy, 19:367–374.
Egelman, E.H., and Stasiak, A. (1986) Structure of helical recA-DNA complexes formed in the presence of ATP-gamma-S and ATP. J. Mol. Biol., 191:677–697.
Egelman, E.H., Francis, N., and DeRosier, D.J. (1983) Helical disorder and the filament structure of F-actin are elucidated by the angle layered aggregate. J. Mol. Biol., 166:605–629.
Elliott, A., and Bennett, P.M. (1984) Mollecular organisation of paramyosin in the core of molluscan thick filaments. J. Mol. Biol., 176:477–493.
Erickson, H.A., and Klug, A. (1971) Measurement and compensation of defocusing and aberrations by Fourier processing of electron micrographs. Philos. Trans. R. Soc. Lond. [B], 261:105–118.
Finch, J.T. (1972) The hand of the helix of tobacco mosaic virus. J. Mol. Biol., 66:291–294.
Finch, J.T., and Klug, A. (1971) Three-dimensional reconstruction of the stacked disc aggregate of tobacco mosaic virus from electron micrographs. Philos. Trans. R. Soc. Lond. [B], 261:211–219.
Finch, J.T., and Klug, A. (1972) The helical surface lattice of bacterial flagella. In: The Generation of Subcellular Structure. R. Markam and J.B. Bancroft (eds). North Holland, Amsterdam, pp. 167–177.
Fraser, D. (1974) Array permutation by index-digit permutation. J. Assoc. Comput. Mach., 23:298–309.
Fraser, R.D.B., and MacRae, T.P. (1973) Conformation in Fibrous Proteins. Academic Press, New York.
Frey, T.G., Eisenberg, D., and Eiserling, F.A. (1975) Proc. Natl. Acad. Sci. USA, 72:3402–3406.
Garrell, R.L., Crepeau, R.H., and Edelstein, S.J. (1979) Cross-sectional views of hemoglobin S fibres by electron microscopy and computer modelling. Proc. Natl. Acad. Sci. USA, 76:1140–1144.
Glaeser, R.W. (1985) Electron crystallography of biological macromolecules. Annu. Rev. Phys. Chem., 36:243–275.
Henderson, R., Baldwin, J.M., Downing, K.H., Lepault, J., and Zemlin, F. (1986) Structure of purple membrane from Halobacterium halobium: Recording, measurement and evaluation of electron micrographs at 3.5 A resolution. Ultramicroscopy, 19:147–178.
Jahnke, E., and Emde, F. (1945) Tables of Functions. Dover, New York.
Kamiya, R., Asakura, S., Wakabayashi, K., and Namba, K. (1979) Transition of bacterial flagella from helical to straight forms with different subunit arrangements. J. Mol. Biol., 131:725–742.
Kato, S., Okamoto, M., and Asakura, S. (1984) Polymorphic transition of the flagellar polyhook from *Escherichia coli* and *Salmonella typhimurium*. J. Mol. Biol., 173:463–476.
Kensler, R.W., and Stewart, M. (1983) Frog skeletal muscle thick filaments are 3-stranded. J. Cell Biol., 96:1797–1802.
Kensler, R.W., and Stewart, M. (1986) An ultrastructural study of crossbridge arrangement in the frog thigh muscle thick filament. Biophys. J., 49:343–351.
Kensler, R.W., Levine, R.J.C., and Stewart, M. (1985) Electron microscopy and optical diffraction study of the structure of scorpion muscle thick filaments. J. Cell Biol., 101:395–401.
Kiselev, N.A., DeRosier, D.J., and Klug, A. (1968) Structure of the tubes of catalase: Analysis of electron micrographs by optical filtering. J. Mol. Biol., 35:561–566.
Klug, A., and DeRosier, D.J. (1966) Optical fitering of electron micrographs: Reconstruction of one-sided images. Nature, 212:29–32.
Klug, A., Crick, F.H.C., and Wycoff, H.W. (1958) Diffraction by helical structures. Acta Crystallogr., 11: 199–213.
Klug, A., Rhodes, D., Smith, J., Finch, J.T., and Thomas, J.O. (1980) A low resolution structure for the histone core of the nucleosome. Nature, 287:509–516.
Laemmli, U., Amos, L.A., and Klug, A. (1976) Correlation between structural transition and cleavage of the major head protein of T4 bacteriophage. Cell, 7:191–203.
Leonard, K., Wingfield, P., Arad, T., and Weiss, H. (1981) Three-dimensional reconstruction of ubiquinol:cytochrome c reductase from neurospora mitochondria determined by electron microscopy of membrane crystals. J. Mol. Biol., 149:259–274.
Lepault, J., and Leonard, K. (1985) Three-dimensional structure of unstained frozen-hydrated extended tails of bacteriophage T4. J. Mol. Biol., 182:431–441.
Lipson, S.G., and Lipson, H. (1969) Optical Physics. Cambridge University Press, Cambridge.
Mandelkow, E.-M., and Mandelkow, E. (1985) Unstained microtubule structure studied by cryo electron microscopy. J. Mol. Biol., 181:123–135.
Mandelkow, E.-M., Schultheiss, R., Rapp, R., Muller, M., and Mandelkow, E. (1986) On the surface lattice of microtubules: Helix starts, protofilament numbers, seams and handedness. J. Cell Biol., 102:1067–1073.
Mellema, J.E., and Klug, A. (1972) Quarternary struc-

ture of gastropod haemocyanin. Nature, 239:146–150.
Milligan, R.A., and Flicker, P.F. (1987) Structural relationships of actin, myosin and tropomyosin revealed by cryo-electron microscopy. J. Cell Biol., 105:29–39.
Misell, D.L. (1978) Image analysis, enhancement and interpretation. In: Practical Methods in Electron Microscopy, Vol. 7. A.M. Glauert, ed. North-Holland, Amsterdam.
Moody, M.F. (1967a) Structure of the sheath of bacteriophage T4. I. Structure of the contracted sheath and polysheath. J. Mol. Biol., 25:177–200.
Moody, M.F. (1967b) Structure of the sheath of bacteriophage T4. II. Rearrangement of the sheath subunits during contraction. J. Mol. Biol., 25:201–208.
Moore, P.B., Huxley, H.E., and DeRosier, D.J. (1971) Three-dimensional reconstruction of F-actin, thin filaments and decorated thin filaments. J. Mol. Biol., 50:279–295.
Namba, K., and Stubbs, G. (1986) Structure of tobacco mosaic virus at 3.6 A resolution: Implications for assembly. Science, 231:1401–1406.
O'Brien, E.J., and Bennett, P.M. (1972) Structure of a straight flagella from a mutant *Salmonella*. J. Mol. Biol., 70:133–152.
O'Brien, E.J., Couch, J., Johnson, G.R.P., and Morris, E.P. (1983) Structure of actin and the thin filament. In: Actin: Its Structure and Function in Muscle and Non-Muscle Cells. C. DosRemedos and J. Barden, eds. Academic Press, New York, pp. 3–16.
Quinlan, R.A., and Stewart, M. (1987) Crystalline tubes of chicken myosin subfragment 2 showing the coiled-coil and molecular interaction geometry. J. Cell Biol., 105:403–415.
Saxton, W.O., and Baumeister, W. (1982) The correlation averaging of a regularly arranged bacterial cell envelope protein. J. Microsc., 127:127–138.
Shirakihara, Y., and Wakabayashi, T. (1979) Three-dimensional image reconstruction of straight flagella from a mutant *Salmonella typhimurium*. J. Mol. Biol., 131:485–507.
Smith, P.R., Aebi, U., Josephs, R., and Kessel, M. (1976) Studies on the structure of the T4 bacteriophage sheath. I. The recovery of three dimensional information from the extended sheath. J. Mol. Biol., 106:243–275.
Smith, P.R., Fowler, W.E., Pollard, T.D., and Aebi, U. (1983) Structure of the actin monomer determined from electron microscopy of crystalline sheets with a tentative alignment of the molecule in the actin filament. J. Mol. Biol., 167:641–660.
Spudich, J.A., Huxley, H.E., and Finch, J.T. (1972) Regulation of skeletal muscle contraction. II. Structural studies on the interaction of the troponin-tropomyosin complex with actin. J. Mol. Biol., 72:619–632.
Steven, A.C., Couture, E., Aebi, U., and Showe, M.K. (1976) Structure of T4 polyheads. II. A pathway of polyhead transformations as a model for T4 capsid maturation. J. Mol. Biol., 106:187–221.
Steven, A.C., Bisher, M.E., Trus, B.L., Thomas, D., Zang, J.M., and Cowell, J.L. (1986) Helical structure of *Bordetella pertusis* fimbriae. J. Bacteriol., 167:968–974.
Stewart, M. (1986) Computer analysis of ordered microbiological objects. In: Ultrastructure Techniques for Microorganisms. H.C. Aldrich and W.J. Todd, eds. Plenum, New York, pp. 333–364.
Stewart, M. (1988) Introduction to the computer image processing of electron micrographs of two-dimensionally ordered biological structures. J. Electron Microscr. Tech., 9:301–324.
Stewart, M., and Murray, R.G.E. (1982) Structure of the regular surface layer of *Aquaspirillum serpens* MW5. J. Bacteriol., 150:348–357.
Stewart, M., and Kensler, R.W. (1986) Arrangement of myosin heads in relaxed thick filaments from frog skeletal muscle. J. Mol. Biol., 192:831–851.
Stewart, M., and Vigers, G. (1986) Electron microscopy of frozen hydrated biological material. Nature, 319: 631–636.
Stewart, M., Kensler, R.W., and Levine, R.J.C. (1981) Structure of *Limulus* telson muscle thick filaments. J. Mol. Biol., 153:781–790.
Stewart, M., Beveridge, T.J., and Sprott, G.D. (1985a) Crystalline order to high resolution in the sheath of *Methanospirillum hungatei:* A cross beta structure. J. Mol. Biol., 183:509–515.
Stewart, M. Kensler, R.W., and Levine, R.J.C. (1985b) Three-dimensional reconstruction of thick filaments from *Limulus* and scorpion muscle. J. Cell Biol., 101:402–411.
Taylor, K.A., and Amos, L.A. (1981) A new model for the geometry of the binding of myosin crossbridges to muscle thin filaments. J. Mol. Biol., 147:297–324.
Taylor, K.A., Dux, L., and Martinosi, A. (1984) Structure of vanadate-induced crystals of sarcoplasmic reticulum. J. Mol. Biol., 174:193–204.
Thon, F. (1966) Zur Defokussierungsabhangigkeit des Phasenkontrastes bei der elektronmikroskopischen Abbildung. Z. Naturforschung, 21a:476–478.
Tokunaga, M., Sutoh, K., Toyoshima, C., and Wakabayashi, T. (1987) Location of the ATP-ase site of myosin determined by three-dimensional electron microscopy. Nature, 329:635–638.
Trachtenberg, S., and DeRosier, D.J. (1987) Three-dimensional structure of the frozen-hydrated flagellar filament. The left-handed filament of *Salmonella typhimurium*. J. Mol. Biol., 195:581–601.
Trachtenberg, S., DeRosier, D.J., and Macnab, R.M. (1987) Three-dimensional structure of the complex flagellar filament of *Rhizobium lupini* and its relation to the structure of the plain filament. J. Mol. Biol., 195:603–620.
Trinick, J., Cooper, J., Seymour, J., and Egelman, E.H. (1986). Cryo electron microscopy and three-dimensional reconstruction of actin filaments. J. Microsc., 141:349–360.
Trus, B.L., and Steven, A.C. (1984) Diffraction patterns from stained and unstained helices: Consistency or contradiction? Ultramicroscopy, 15:325–336.
Unwin, P.N.T. (1974) Electron microscopy of the stacked disc form of tobacco mosaic virus. II. The influence of electron irradiation on stain distribution. J. Mol. Biol., 87:657–670.
Unwin, P.N.T., and Klug, A. (1974) Electron microscopy of the stacked disc form of tobacco mosaic virus. I. Three-dimensional reconstruction. J. Mol. Biol., 87:641– 656.
Vainstein, B.K. (1966) Diffraction of X-Rays by Chain Molecules. Elsevier, Amsterdam.
Vibert, P.J., and Craig, R. (1982) Three-dimensional reconstruction of thin filaments decorated with a Ca-regulated myosin. J. Mol. Biol., 157:299–319.
Vibert, P.J., and Craig, R. (1983) Electron microscopy and image analysis of myosin filaments from scallop striated muscle. J. Mol. Biol., 165:303–320.
Wagenknecht, T., DeRosier, D.J., Shipiro, L., and Weissborn, A. (1981) Three-dimensional reconstruction of the flagellar hook of *Caulbacter crescentus*. J. Mol. Biol., 151:439–465.
Wakabayashi, T., and Toyoshima, C. (1981) Three-dimensional image analysis of the complex of thin

filaments and myosin molecules from skeletal muscle. J. Biochem. (Tokyo), 90:683–701.
Wakabayashi, T., Huxley, H.E., Amos, L.A., and Klug, A. (1975) Three-dimensional image reconstruction of actin-tropomyosin complex and actin-tropomyosin-troponin-T-troponin-I complex. J. Mol. Biol., 93:477–497.
Wischik, C.M., Crowther, R.A., Stewart, M., and Roth, M. (1985) Subunit structure in paired helical filaments in Alzheimer's disease. J. Cell Biol., 100:1905–1912.
Yanagida, M., DeRosier, D.J., and Klug, A. (1972) The structure of the tubular variants of the head of bacteriophage T4 (polyheads). II. Structural transition from a hexamer to a 6 + 1 morphological unit. J. Mol. Biol., 65:489–499.